Tensor-network renormalization approach to the q-state clock model

Guanrong Li, Kwok Ho Pai, and Zheng-Cheng Gu*
Department of Physics, The Chinese University of Hong Kong, Shatin, New Territories, Hong Kong, China

(Received 5 August 2021; accepted 17 February 2022; published 31 May 2022)

We simulate the phase diagram and critical behavior of the q-state clock model on the square lattice by using the state-of-the-art loop optimization for tensor-network renormalization (loop-TNR) algorithm. The two phase transition points for $q \geqslant 5$ are determined with very high accuracy. Furthermore, by computing the conformal scaling dimensions for both transition points, we are able to determine the radius R of the compactified boson theories at both transition points with high precision. In particular, the radius R at higher temperature phase transition point is precisely the same as the one predicted by Berezinskii-Kosterlitz-Thouless (BKT) transition. Moreover, we find that the fixed-point tensors at higher temperature transition point also converge to the same one approximately for large enough q and the corresponding operator product expansion (OPE) coefficient of the compactified boson theory can also be read out directly from the fixed-point tensor.

DOI: 10.1103/PhysRevResearch.4.023159

I. INTRODUCTION

Berezinskii-Kosterlitz-Thouless (BKT) [1–3] transition was originally proposed in classical XY model with a continuum U(1) symmetry. It is well known that spontaneous breaking of continuum symmetry is not allowed in 2D classical systems and the BKT transition provides us the first example beyond Landau's symmetry breaking paradigm. On the contrary, spontaneous breaking of discrete symmetry is generally allowed for 2D classical systems and BKT transition is usually not expected for these systems. In recent years, researchers have found very strong numerical evidence that BKT transition indeed also happens in systems with discrete symmetry, e.g., the q-state clock model [4]. It has been pointed out that for $q \geqslant 5$, the q-state clock model typically has two critical points [5]. At the high-temperature critical point, the system undergoes a BKT transition, while at the low-temperature critical point, the long-range order would emerge and the usual symmetry breaking transition happens. Theoretically, it has been well known that q-state model with large enough q is effectively described by Z_q deformed sine-Gordon model [6], and the renormalization analysis also suggests that the model will undergo two phase transitions as the temperature decreases. Between the two phase transition points, the effective field theory reduced to a simple compactified boson theory with emergent U(1) symmetry. Previously, a number of studies have been focused on how to determine the two critical temperatures [7–16], but how to extract the exact conformal data at critical points is still very challenging. Although recently there is some progress on computing compactification radius, the operate product expansion (OPE) coefficient is still impossible with the current numerical techniques [17–29].

Tensor renormalization group (TRG) or tensor entanglement filtering renormalization group (TEFRG) algorithm [30,31] is a powerful tool to study the phase diagram of 2D classical statistical models. By investigating the properties of the corresponding fixed-point tensor for off-critical systems, the phase diagram can be read out directly. However, for critical systems, the conformal data such as central charge and scaling dimensions are still not accurate enough and seriously suffer from the stability problem after a few renormalization group (RG) steps. In recent years, by eliminating short-range quantum entanglement, tensor-network renormalization (TNR) [32] algorithm was first proposed as real space renromalization group method to improve the accuracy and stability of conformal data. Subsequently, the so-called loop optimization for tensor-network renormalization (loop-TNR) [33] was developed to significantly increase the efficiency of TNR scheme. Comparing with other singular value decomposition based methods, such as TRG/TEFRG and higher order TRG (HOTRG) [34,35], the loop-TNR algorithm provides us much more precise and stable conformal data for critical systems.

In this paper, we use loop-TNR algorithm to study the phase transition properties of the q-state clock model. We find very strong numerical evidence that the physics of self-dual critical points for $q < 5$ model matches very well with the previous proposal from conformal field (CFT) theory and other numerical results. For $q \geqslant 5$ model, the middle phase between the symmetry-breaking transition point and BKT critical point is described by the compactified boson theory with central charge $c = 1$. By computing the scaling dimensions of the two transition points as well as the so-called self-dual points, we are able to determine the compactification radius R of the corresponding compactified boson theory with very high accuracy. We find that at both phase transition points as well

*zcgu@phy.cuhk.edu.hk

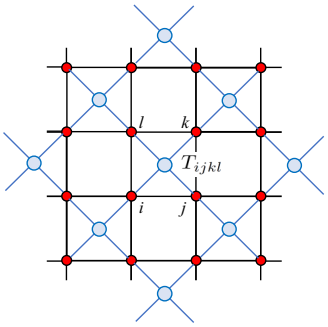

FIG. 1. Tensor-network representation of q-state clock model on square lattice.

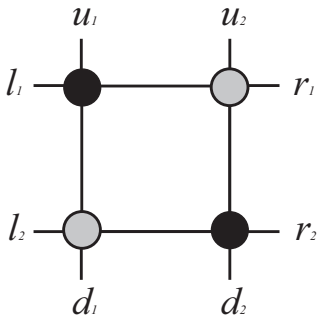

FIG. 2. We use the 2 by 2 block to represent the fixed-point tensor T when calculating χ, where we group the index (i_1, i_2) into a single index i for tensor T.

as self-dual point, the obtained compactification radii R perfectly agree with the field theory predictions. Furthermore, we also find that for big enough q, the corresponding fixed-point tensors at the high-temperature transition point T_{c2} converge to the same one approximately, describing BKT transition with an emergent U(1) symmetry, and the corresponding OPE coefficients of the compactified boson theory can also be read out directly. We stress that our method not only gives critical temperature with very high precision, but also provides us accurate conformal data, especially for the cases with $q = 5$ and $q = 6$, which are very hard to be simulated by density matrix renormalization group (DMRG)/matirx product state (MPS) based methods [11,29] as well as Monte Carlo (MC) simulation [7,9,10,14,20,21,23,24,27,28] due to the presence of marginal irrelevant terms [36]. Our numerical results also suggest that 2D CFT could be reformulated as an infinite dimensional fixed-point tensor, which encodes the complete conformal data, such as scaling dimensions and OPE coefficients. This might lead to an algebraic way to reformulate and classify all 2D CFT.

II. TENSOR-NETWORK RENORMALIZATION FOR q-STATE CLOCK MODEL

The q-state clock model is describe by the Hamiltonian

$$H = -J\sum_{\langle ij\rangle}\cos(\theta_i - \theta_j), \tag{1}$$

where $\theta_i = 2\pi n_i/q$, and $n_i \in \{1, 2, ...q\}$. We note that for $q = 2$ and $q = 3$ the model is equivalent to classical Ising model and 3-states Potts model. The partition function of the q-state clock model can be expressed as a trace of local tensors:

$$Z = \mathrm{Tr}e^{-\beta H} = \sum_{ijkl\cdots}\prod T_{ijkl} \equiv \mathrm{tTr}\otimes T. \tag{2}$$

As seen in Fig. 1, we use red dots to represent the original square lattice, and the tensor T_{ijkl} is defined on the dual lattice with light blue dots. Here we consider systems with periodic boundary condition (PBC) with all edges of the dual lattice are summed over. The element tensor T_{ijkl} is defined as

$$T_{ijkl} = \exp\beta(\cos\theta_{ij} + \cos\theta_{jk} + \cos\theta_{kl} + \cos\theta_{li}), \tag{3}$$

where $\theta_{ij} = 2\pi(i - j)/q$ and i, j, k, l take values $\{1, 2, ...q\}$. Below we will use the loop-TNR algorithm [33] to determine the critical points of this model and compute the corresponding conformal data.

For $q < 5$, it is well known that the self-dual critical temperature reads [37]:

$$\beta_c = \begin{cases} \ln(\sqrt{2}+1)/2, & q = 2 \\ 2\ln(\sqrt{3}+1)/3, & q = 3. \\ \ln(\sqrt{2}+1), & q = 4 \end{cases} \tag{4}$$

We will first benchmark with these exact results to examine the accuracy of our algorithm. Since the $q = 2$ case has already been studied before, here we will begin with the $q = 3$ and $q = 4$ cases. To find the critical point, we first calculate the gauge invariant quantity χ introduced in Ref. [31]:

$$\chi = \frac{\left(\sum_{ij} T_{ijij}\right)^2}{\sum_{ijkl} T_{ijkl}T_{klij}}, \tag{5}$$

where we use the 2 by 2 block to represent the fixed-point tensor T (composed by T_A and T_B on sublattices A and B, respectively) when calculating the gauge invariant quantity χ, as shown in Figs. 2 and 3.

As seen in Fig. 4, we see that there is a sudden jump from ordered phase to disordered phase. This is because the tensors for ordered and disordered phase would flow to different fixed points. To understand better for the gauge invariant quantity χ, we introduce matrix M^h and M^v:

$$M^h_{ij} = \sum_k T^{\text{fixed-point}}_{ikjk}, \quad M^v_{ij} = \sum_k T^{\text{fixed-point}}_{kikj}. \tag{6}$$

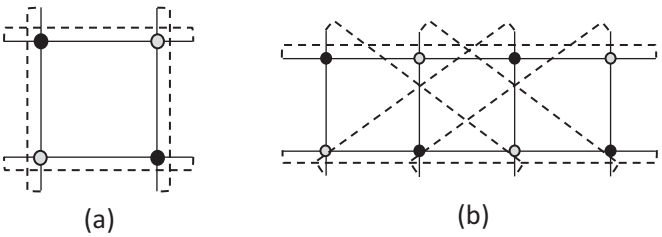

FIG. 3. Gauge invariant quantity χ formed by T, where the numerator is represented by the square of part (a), and the denominator is given by part (b).

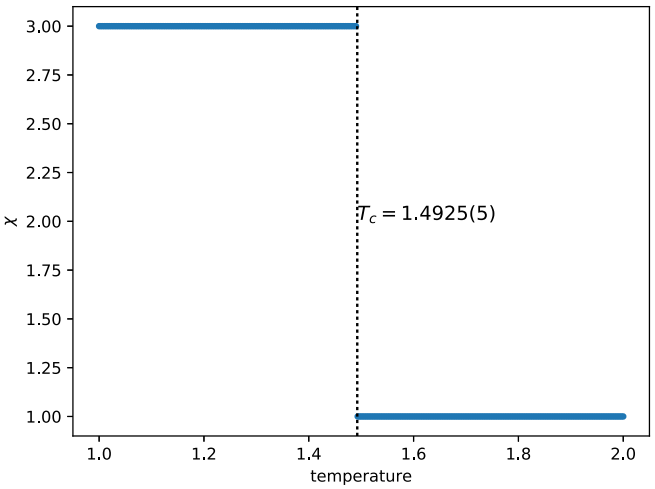

FIG. 4. The invariant quantity χ as a function of temperature. We find that the critical temperature T_c for $q = 3$ model is around 1.4925(5), which agrees with the prediction of the self-dual analysis. Here we keep $D_{\text{cut}} = 36$ in the loop-TNR algorithm and system size up to 2^{23}.

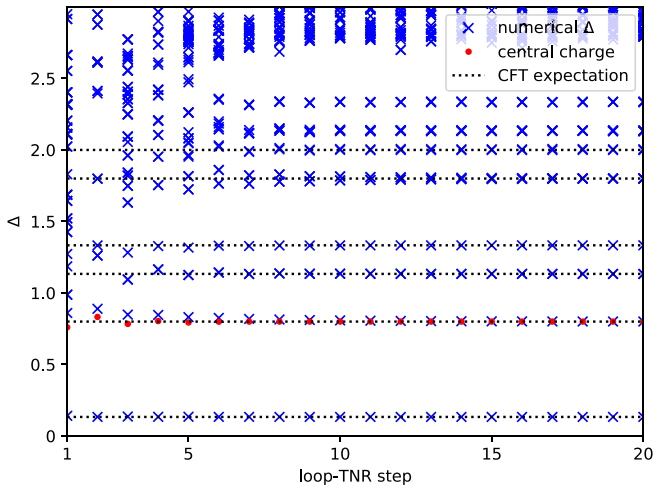

FIG. 5. The scaling dimensions at the critical point of $q = 3$ model with $D_{\text{cut}} = 36$. We see that the conformal data rapidly converges to CFT predictions during the renormalization process.

We see that for ordered phase, the eigenvalue λ of M^h and M^v is

$$\begin{matrix} \lambda_1, \lambda_2, \ldots \lambda_q = 1/q \\ \text{others} \qquad\quad = 0 \end{matrix}. \tag{7}$$

In disordered phase, we have $\lambda_1 = 1$, and all the others approach 0, which shows clearly the symmetry breaking nature of the phase transition. Here, we have already normalized the fixed-point tensor as

$$\sum_{jk} T^{\text{fixed-point}}_{jkjk} = 1. \tag{8}$$

Next, we compute the central charge and scaling dimensions (we keep $D_{\text{cut}} = 36$ in our loop-TNR algorithm). We find that the central charge $c = 0.80005$, which agrees pretty well with the value predicted by the CFT with $c = 4/5$. In Fig. 5, we see that both central charge and scaling dimensions are very stable up to 20 renormalization steps, which corresponds to a total system size 2^{23}.

Similarly, we can compute the gauge invariant quantity χ, central charge and scaling dimensions for the $q = 4$ model (again, we keep $D_{\text{cut}} = 36$ in our loop-TNR algorithm), as shown in Figs. 6 and 7. We find that $c = 1.00021$, which is also consistent with previous theoretical predictions. In fact, the critical point of $q = 4$ model can be just regarded as two copies of the Ising CFT. Again, we see that both central charge and scaling dimensions are very stable up to 20 renormalization steps.

III. $q = 5$ AND $q = 6$ MODELS

For $q \geqslant 5$, it is conjectured that the q-state clock model is described by Z_q-deformed sine-Gordon theory [4,6]

$$S = \frac{1}{2\pi K}\int d^2\mathbf{r}(\nabla\phi)^2 + \frac{g_1}{2\pi\alpha^2}\int d^2\mathbf{r}\cos(\sqrt{2}\phi) + \frac{g_2}{2\pi\alpha^2}\int d^2\mathbf{r}\cos(q\sqrt{2}\Theta), \tag{9}$$

where ϕ, Θ are compactified as $\phi \equiv \phi + \sqrt{2}\pi$, $\Theta \equiv \Theta + \sqrt{2}\pi$, and they satisfy the dual relation $\partial_x\phi = -K\partial_y\Theta$, $\partial_y\phi = K\partial_x\Theta$. The coupling constants K, g_1, g_2 are temperature dependent, and α is a UV cutoff.

With decreasing temperature, the above effective theory will describe two phase transitions, which can be understood from the renormalization group flow of the second and third terms. The high-temperature critical point is described by the well known BKT transition while the low-temperature transition is described by the usual symmetry breaking transition. As the coupling g_1 and g_2 become irrelevant between the two critical points $T_{c1} < T < T_{c2}$, the effective theory reduced to compactified boson theory in the middle phase, with compactification radius $R = \sqrt{2K}$. In addition, if $g_1 = g_2$, Eq. (9) is self-dual. From the scaling dimension analysis, the

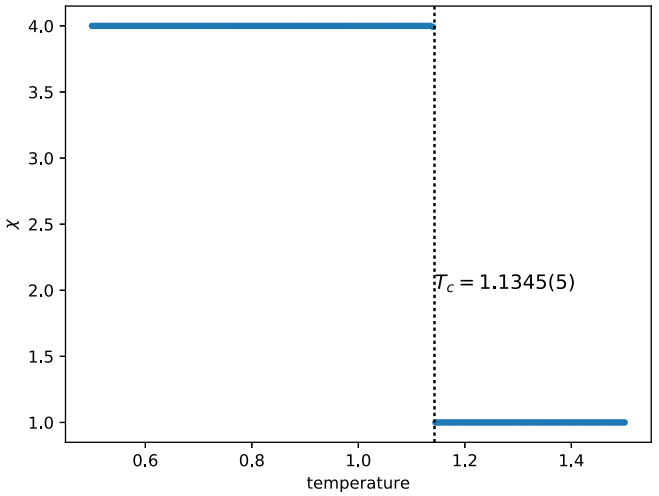

FIG. 6. The invariant quantity χ as a function of temperature. We find that the critical temperature T_c for $q = 4$ model is around 1.1345(5), which also agree with the prediction of the self-dual analysis [37]. Here we also keep $D_{\text{cut}} = 36$ in the loop-TNR algorithm and system size up to 2^{23}.

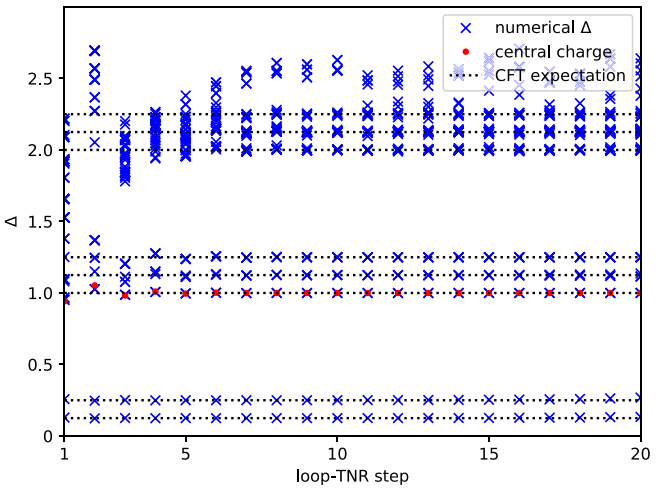

FIG. 7. The scaling dimensions at the critical point of $q = 4$ model with $D_{\text{cut}} = 36$.

compactification radius can be computed exactly for both phase transition points as well as for the self-dual point [29]. We have:

$$R_{c2} = 2\sqrt{2}, \text{ BKT transition point}$$
$$R_{\text{self-dual}} = \sqrt{2q}, \text{ self-dual point}$$
$$R_{c1} = q/\sqrt{2}, \text{ symmetry-breaking point.}$$

Similar to the $q < 5$ model, two transition points of $q = 5$ model can be read out from the gauge invariant quantity χ. In Fig. 8, we plot χ as a function of temperature near the critical point. Very different from the $q < 5$ model, there is no sharp change in χ near the two phase transition points. Similar to the $q < 5$ model, in ordered phase, the tensor would flow to the fixed point with $\chi = 5$, while in disordered phase, the fixed-point tensor gives rise to $\chi = 1$. However, in the middle phase, the structure of fixed-point tensor is very complicated and we will discuss the details later. An interesting feature is that the gauge invariant quantity χ becomes size independent in the middle critical phase and this help us pin down the critical temperature for both high-temperature and low-temperature phase transitions. As seen from Fig. 8, we can read out that the low-temperature symmetry breaking transition point T_{c1} is around 0.909(1) while the high-temperature BKT phase transition point is around 0.949(1). Similar analysis can be applied to $q = 6$ model as well, and we can read out from Fig. 9 that the low-temperature critical point T_{c1} is around 0.699(1), and high-temperature phase transition point T_{c2} is around 0.909(1). In order to increase the stability of accuracy, here and below we will use the Z_q symmetric loop-TNR algorithm (see Appendix D for more details) with D_{cut} being the integer multiple of q, and $60 < D_{\text{cut}} < 70$ for simulating all q-state clock models.

Since the middle phase is described by compactified boson model, we can further use the fixed-point tensor to compute its central charge and scaling dimensions. As seen in Fig. 10, we find $c = 0.99987$ for $q = 5$ model with $T = 0.93k_B/J$, which agree pretty well with the theoretical prediction with $c = 1$. It is well known that the scaling dimension of the primary fields

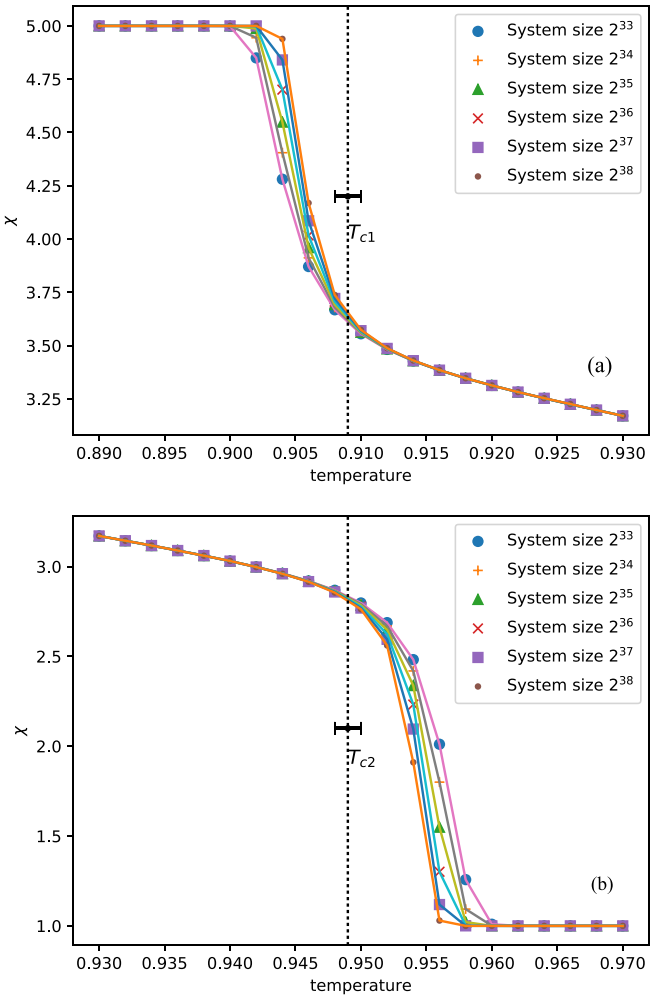

FIG. 8. Invariant quantity of $q = 5$ model around T_{c1} and T_{c2}. We can read that $T_{c1} = 0.909(1)$, and $T_{c2} = 0.949(1)$, with the same analysis with $q = 5$ model.

of the compactified boson model can be expressed as

$$\Delta_{e,m} = \frac{m^2}{R^2} + \frac{e^2R^2}{4}, \tag{10}$$

where R is the compactified radius and m, e are integers, which label the primary fields. In Fig. 10, we also plot the scaling dimension for $q = 5$ model with $T = 0.93k_B/J$. We find that all the low-scaling dimension can be fit quite well with $R = 3.08607$. Here we choose the scaling dimensions of RG steps from 15–20 to fit the compactification radius R, see Appendix A for more details. We note that the deviations for high-scaling dimensions are due to the numerical error and we can further improve the accuracy by increasing D_{cut} in the loop-TNR algorithm.

The BKT transition point T_{c2} can also be determined by the susceptibility peak method with extremely high accuracy. First, by applying a very small external field, we can compute the susceptibility at different external field h and temperature T [38]:

$$\chi(h, T) = \left.\frac{\partial m}{\partial h}\right|_T. \tag{11}$$

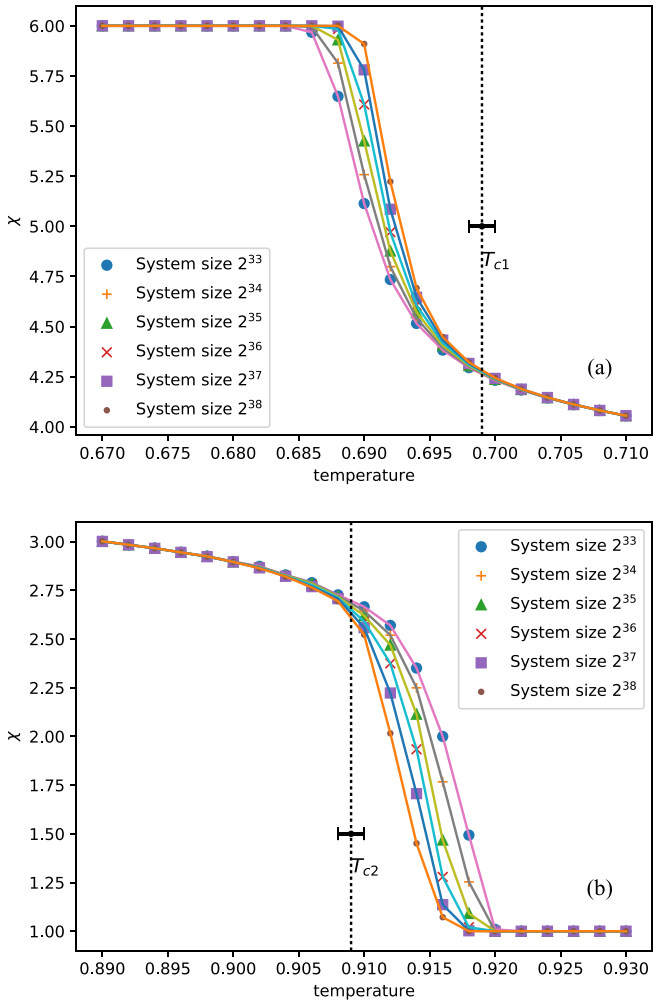

FIG. 9. Invariant quantity of $q = 6$ model around T_{c1} and T_{c2}. We can read that $T_{c1} = 0.699(1)$, and $T_{c2} = 0.909(1)$, with the same analysis with $q = 6$ model.

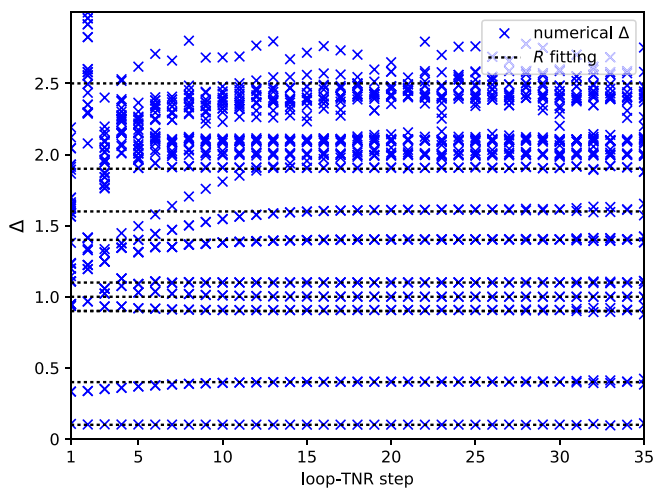

FIG. 10. An example of scaling dimensions in the critical phase for $q = 5$ model.

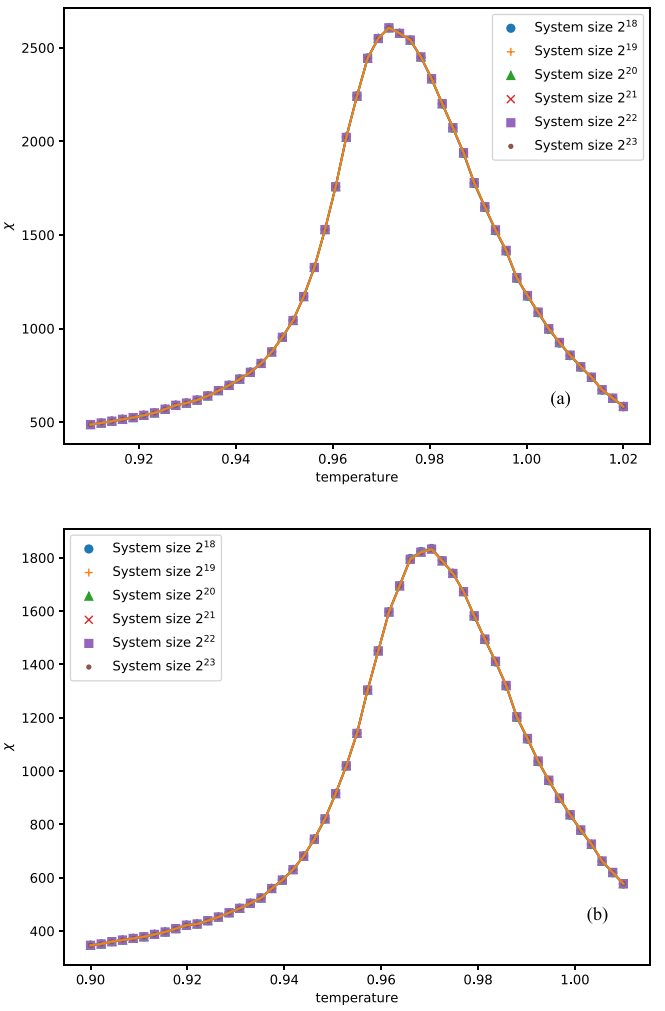

FIG. 11. Susceptibility of (a) $q = 5$ and (b) $q = 6$ models with external field $h = 10^{-5}$.

For example, in Fig. 11, we plot the susceptibility function at different system size for $q = 5$ and $q = 6$ models with a very small external field $h = 10^{-5}$. We see that all the susceptibility functions collapse to a single curve, which implies that the thermodynamic limit has already been achieved for physical quantities, despite to the fact that the gauge invariant quantity χ still has very strong size dependence near both critical temperatures. If we assume that the high-temperature transition is indeed KBT type, the susceptibility peak temperature should approach T_{c2} as a power law function with respect to the external fields. By plotting the peak position of χ with different external fields and extrapolating the peak temperature to the $h = 0$ limit, we can read out T_{c2} by using the following formula [38]:

$$T_{\text{peak}}(h) - T_c = ah^b. \tag{12}$$

We find that for $q = 5$ model, $T_{c2} = 0.9507(5)$, $a = 0.5605$, $b = 0.3028$, and for $q = 6$ model, $T_{c2} = 0.9111(5)$, $a = 0.4057$, $b = 0.1662$. Figures 12 and 13 show the susceptibility-peak fitting for $q = 5$ and $q = 6$ models, respectively. We see that the results of T_{c2} is comparable with what we get from the gauge invariant quantity χ.

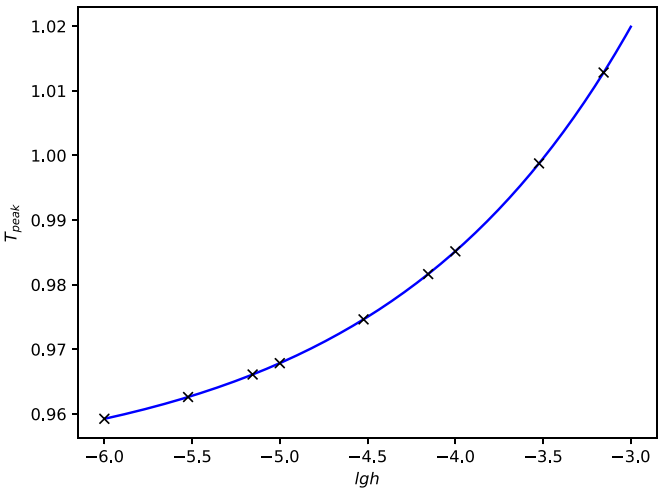

FIG. 12. Susceptibility peak temperature versus external field for $q = 5$ model, from which we find that $T_c = 0.9507(5)$, $a = 0.5605$, $b = 0.3028$.

In Table I, we compare our results with all previous known results for T_{c1} and T_{c2} using other methods. We see that our method gives much more precise critical temperatures than HOTRG based method [13,15], and the results are comparable with recent MPS based method [29] and large scale M.C. results [23,28]. We note that the small disagreement in the last digit might arise from the finite-size effect in other methods. Our loop-TNR method can handle system size up to 2^{23} with very high accuracy.

We further compute the scaling dimensions at T_{c1} and T_{c2} for of both $q = 5$ and $q = 6$ models. From the results of scaling dimension at each RG step, we can clearly observe the logarithmic flow of some higher scaling dimensions, as seen in Figs. 14 and 15. This implies the existence of marginal irrelevant terms [36] for these transition points, and it explains why these transition points are very hard to be determined precisely in previous studies. From the scaling dimensions,

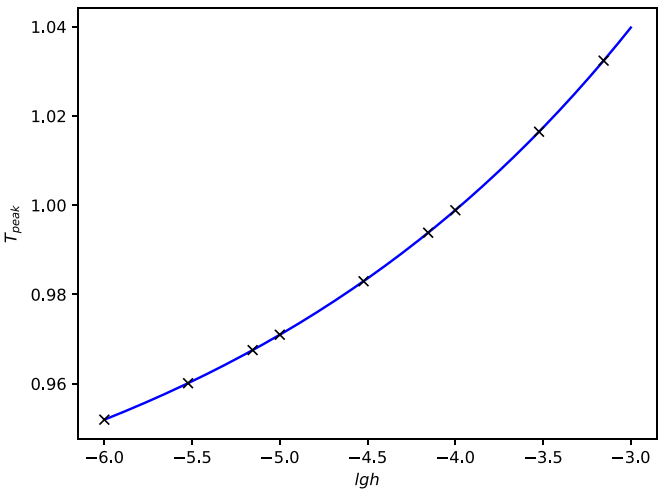

FIG. 13. Susceptibility peak temperature vs external field for $q = 6$ model, from which we find that $T_c = 0.9111(5)$, $a = 0.4057$, $b = 0.1662$.

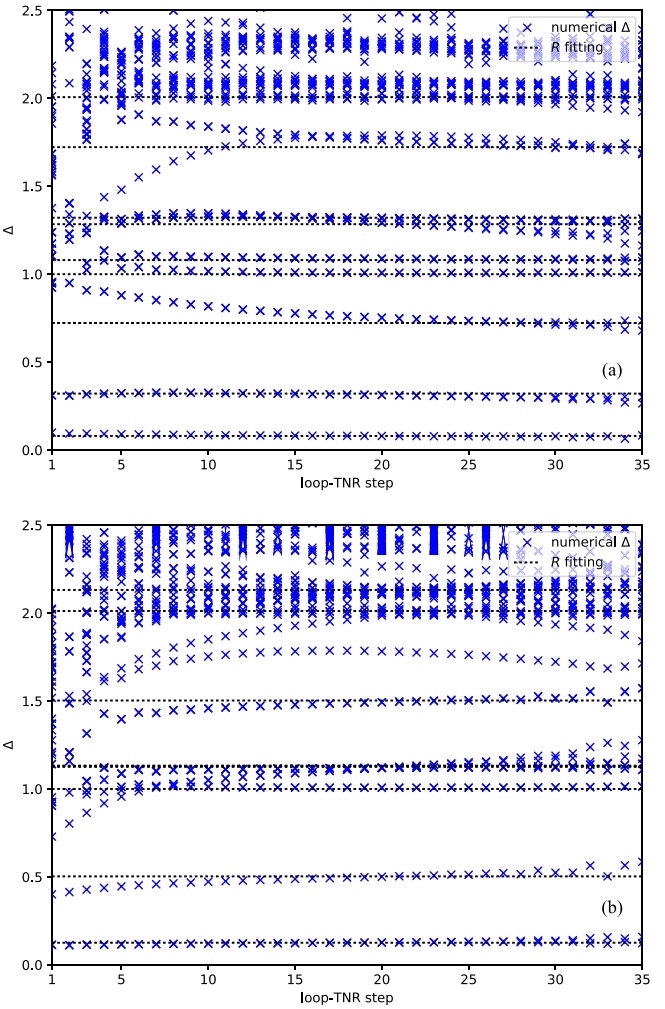

FIG. 14. Scaling dimensions at the critical point (a) T_{c1} and (b) T_{c2} for $q = 5$ model, from which we can fit the compactification radius R of the compactified boson theory. We find that at T_{c1}, $R = 3.52954$, and at T_{c2}, $R = 2.83894$.

we can fit the compactification radius R by using Eq. (10). In Table II, we list the compactification radius R at both transition points and we find a perfect agreement with the field theory predictions. We see that comparing with the very recent studies by using MPS based method [29], our results give rise to much more precise compactification radius R at these phase transition points. In addition, we also computed the scaling dimensions and fit compactification radius R in Table II for the so-called self-dual point, see Appendix B for more details.

IV. $q > 6$ MODELS AND FIXED-POINT TENSOR FOR BKT TRANSITION

A. Critical temperature and compactification radius

By using the same methods for $q = 5$ and $q = 6$ models, we also studies the phase diagram for $q > 6$ models. By computing both the gauge invariant quantity χ and fitting the susceptibility peak position under different external field, we can determine both T_{c1} and T_{c2} with very high precision (see Appendix C for more details). In Table III, we compare our results for $q = 7, 8, 9$ models with previous studies using

TABLE I. A comparison of T_{c1} and T_{c2} with previous results by using other methods.

Reference	Method	T_{c1}	T_{c2}
	$q = 5$		
Tobochnik [7]	MCRG	0.8	1.1
Borisenko *et al.* [23]	M.C. cluster	0.905(1)	0.951(1)
Kumano *et al.* [10]	Boundary-flip M.C.	0.908	0.944
Chatelain [11]	DMRG	0.914(12)	0.945(17)
Chatterjee *et al.* [27]	Swendsen-Wang M.C.	0.897(1)	
Chen *et al.* [15]	HOTRG	0.9029(1)	0.9520(1)
Surungan *et al.* [28]	CTMRG	0.911(5)	0.940(5)
Hong and Kim [16]	HOTRG	0.908	0.945
Li *et al.* [29]	VUMPS	0.9059(2)	0.9521(2)
Our result	loop-TNR (gauge invariant quantity χ)	0.909(1)	0.949(1)
	loop-TNR (magnetic susceptibility)	-	0.9507(5)
	$q = 6$		
Tobochnik [7]	MCRG	0.6	1.3
Challa and Landau [17]	M.C.	68(2)	0.92(1)
Yamagata and Ono [19]	M.C.	0.68	0.90
Tomita and Okabe [20]	Probability-changing cluster M.C.	0.7014(11)	0.9008(6)
Hwang [21]	Wang-Landau M.C.	0.632(2)	0.997(2)
Brito *et al.* [22]	Heat-bath single spin flipping M.C.	0.68(1)	0.90(1)
Baek *et al.* [26]	Wolff M.C.		0.9020(5)
Kumano *et al.* [10]	Boundary-flip M.C.	0.700(4)	0.904(5)
Krčmár *et al.* [12]	CTMRG	0.70	0.88
Chen *et al.* [13]	HOTRG	0.6658(5)	0.8804(2)
Chatterjee *et al.* [27]	Swendsen-Wang M.C.	0.681(1)	
Surungan *et al.* [28]	CTMRG	0.701(5)	0.898(5)
Hong and Kim [16]	HOTRG	0.693	0.904
Li *et al.* [29]	VUMPS	0.6901(4)	0.9127(5)
Ueda *et al.* [39]	CTMRG (correlation length etc.)	0.694(3)	0.908(3)
	CTMRG (entanglement Spectrum)	0.693	0.900
Krčmár *et al.* [40]	CTMRG (entanglement entropy)	0.70	0.88
Our results	loop-TNR (gauge invariant quantity χ)	0.699(1)	0.909(1)
	loop-TNR (magnetic susceptibility)		0.9111(5)

other methods. Remarkably, for models with big enough q, i.e., $q > 6$, T_{c2} becomes very close to the BKT transition value in classical XY model with $T_c = 0.8929$.

Similar to $q = 5$ and $q = 6$ models, we can also use loop-TNR method to compute the scaling dimensions and fit the corresponding compactification radius R (see Appendix C for more details). We find that the radius R at T_{c2} also saturates to a fixed value 2.81987 for big enough q, which agree pretty well with the theoretical prediction $R = 2\sqrt{2}$. We can also use the same method for $q = 5$ and $q = 6$ models to determine the self-dual point and fit the corresponding compactification radius R. In Table IV, we also list the compactification radius R for T_{c1} and self-dual point T_{dual}. Again, all the values agree pretty well with theoretical predictions.

TABLE II. Compactification radius R on both critical points as well as self-dual point of q-state clock model with $q = 5$ and $q = 6$.

	T_{c1}		T_{dual}		T_{c2}	
q	Theory	Numerical	Theory	Numerical	Theory	Numerical
5	$\sqrt{25/2}$	3.52954	$\sqrt{10}$	3.17354	$2\sqrt{2}$	2.83894
6	$\sqrt{18}$	4.23870	$\sqrt{12}$	3.46002	$2\sqrt{2}$	2.82024

B. Fixed-point tensor for BKT transition

Since the T_{c2} for $q > 6$ models is already very close to the BKT transition in classical XY model, and the compactification radius R is also approaching the expected value for BKT transition, it is natural to ask whether the corresponding fixed point tensors in these models also converge to the same one approximately or not? Below we will study the structure of fixed point tensor for $q > 6$ models at BKT transition and try to read out the (leading) OPE coefficients of primary fields directly for the corresponding compactified boson CFT. We note that Ref. [41] proposed a more generic method to compute the OPE coefficient in TNR-based algorithm, however, here our major purpose is to understand the structure of the fixed-point tensor.

1. The gauge choice of the fixed-point tensor

It is well known that there exists a gauge degree of freedom for the fixed-point tensor in any TNR based scheme and it

TABLE III. A comparison of T_{c1} and T_{c2} with previous results by using other methods.

Reference	Method	T_{c1}	T_{c2}
	$q = 7$		
Borisenko [24]	M.C.	0.533	0.900
Chatterjee *et al.* [27]	Swendsen-Wang M.C.	0.531(6)	
Li *et al.* [29]	VUMPS	0.5305(3)	0.9071(5)
Our results	loop-TNR (gauge invariant quantity χ)	0.537(1)	0.899(1)
	loop-TNR (magnetic susceptibility)		0.9065(5)
	$q = 8$		
Tomita and Okabe [20]	Probability-changing cluster M.C.	0.4259(4)	0.8936(7)
Baek *et al.* [8]	M.C.	0.417(3)	0.894(1)
Chatterjee *et al.* [27]	Swendsen-Wang M.C.	0.418(1)	
Li *et al.* [29]	VUMPS	0.4172(3)	0.9060(5)
Our results	loop-TNR (gauge invariant quantity χ)	0.423(1)	0.899(1)
	loop-TNR (magnetic susceptibility)		0.9051(5)
	$q = 9$		
Chatterjee *et al.* [27]	Swendsen-Wang M.C.	0.334(1)	
Our results	loop-TNR (gauge invariant quantity χ)	0.341(1)	0.899(1)
	loop-TNR (magnetic susceptibility)		0.9051(5)

is actually the major difficulty for us to understand the full structure of fixed-point tensors for critical systems.

We will begin with some general discussion for the nature of such a gauge degree of freedom and explain why it can be fixed by introducing enough symmetry conditions. Apparently, if we apply some invertible matrices on every legs of a tensor, the transformed tensor actually forms the same tensor network as before:

$$T'_{ijkl} = \sum_{i'j'k'l'} T_{i'j'k'l'} U_{i'i} V_{j'j} [U^{-1}]_{kk'} [V^{-1}]_{ll'}. \tag{13}$$

This gives rise to great difficulty to analyze the properties of the tensor components of the fixed-point tensor, since they could be randomly affected by the gauge choice in numerical calculations. To get a proper gauge fixing, we have the following considerations:

(i) The fixed-point tensor (defined on the 2 by 2 plaquette composed by T_A and T_B tensors, as shown in Fig. 2) should preserve the C_4 lattice symmetry during the loop-TNR process (see Appendix D for more details). Preserving C_4 symmetry will reduce the gauge freedom of the fixed-point tensor. The gauge transformation in Eq. (13) can be simplified as

$$T'_{ijkl} = \sum_{i'j'k'l'} T_{i'j'k'l'} O_{i'i} O_{j'j} O_{k'k} O_{l'l}, \tag{14}$$

TABLE IV. Compactification radius R on critical points and self-dual point for $q = 7, 8, 9$ models.

	T_{c1}		T_{dual}		T_{c2}	
q	Theory	Numerical	Theory	Numerical	Theory	Numerical
7	$\sqrt{49/2}$	4.94072	$\sqrt{14}$	3.75035	$2\sqrt{2}$	2.83153
8	$\sqrt{32}$	5.67377	$\sqrt{16}$	4.00726	$2\sqrt{2}$	2.81987
9	$\sqrt{81/2}$	6.36759	$\sqrt{18}$	4.23573	$2\sqrt{2}$	2.81987

where O is an orthogonal matrix. Here we assume all the tensors are real.

(ii) Since the q-state clock model has a Z_q internal symmetry, we should also keep such an internal symmetry during the whole loop-TNR process (see Appendix D for more details). By keeping the Z_q symmetry, we can further reduce the gauge degrees of freedom. In fact this is a crucial step to obtain the right fusion rule for fixed-point tensor. It is well known that the fusion rule of compactified boson theory has a U(1) symmetry, which can be realized explicitly on XY model. However, if we only focus on the leading components of primary fields, Z_q symmetry is a very good approximation for U(1) with big enough q. [Strictly speaking, to eliminate gauge degree of freedoms completely, the exact U(1) symmetry is required, however, for big enough q, the effect of gauge transformations can be neglected for leading primary fields.]

(iii) If we want the indices of the fixed-point tensor to represent the primary fields and their descendants for the corresponding compactified boson theory, we need to choose a proper basis. The eigenstate of the transfer matrix is a good choice. As shown in Fig. 16(d), we construct a rank-3 tensor with the building block tensor M_{ijkl} in C_4-loop-TNR algorithm (see Appendix D for more details). This is because in usual CFT, the 3-point correlation function is more fundamental and has a much simpler form than the 4-point correlation function. In fact, the basic renormalization step in loop-TNR is similar to the crossing symmetry for 4-point correlation function. We conjecture that the rank-4 tensor in the TNR algorithm can be regarded as a 4-point correlation function (with proper boundary conditions), as a result, the decomposition of the rank-4 tensor into the summation of two rank-3 tensors can be naturally regarded as decomposing of a 4-point correlation function into summations of two 3-point correlation functions. Thus, the rank-3 tensor constructed here could be regarded as a 3-point correlation function (at least for primary fields). As illustrated in Fig. 17, we construct the

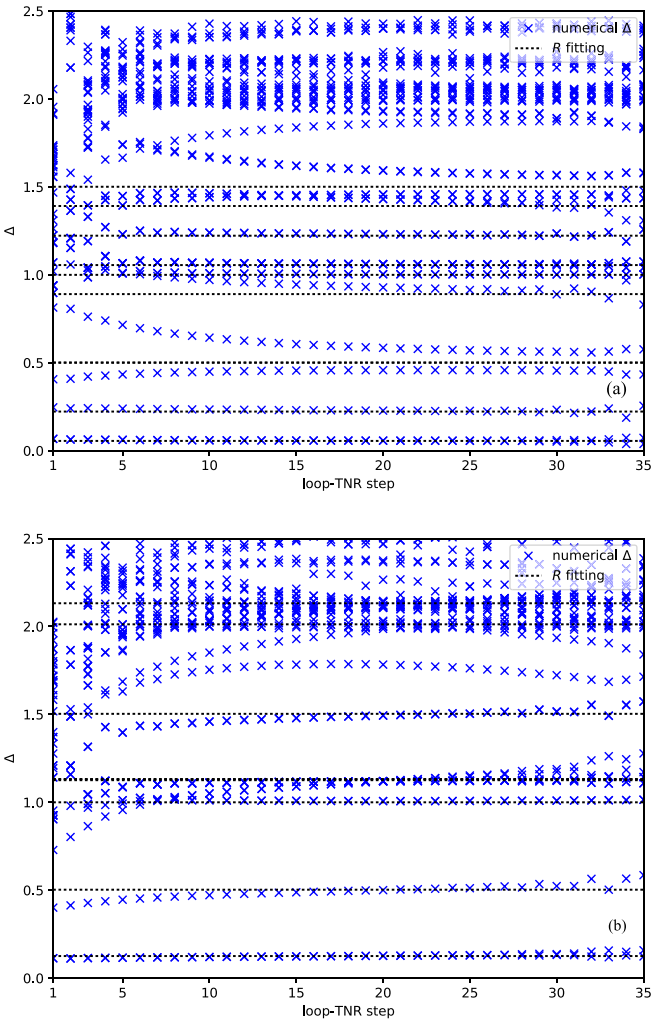

FIG. 15. Scaling dimensions at the critical point (a) T_{c1} and (b) T_{c2} for $q = 6$ model, from which we can fit the compactification radius R of the compactified boson theory. We find that at T_{c1}, $R = 4.23870$, and at T_{c2}, $R = 2.82024$.

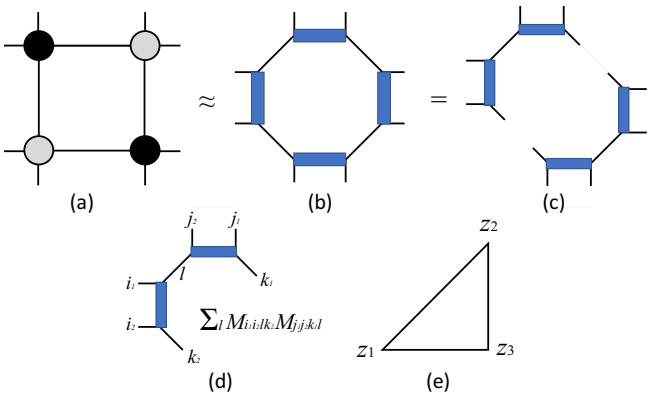

FIG. 16. From loop-TNR algorithm, a square fixed-point tensor (a) could be approximately represented by MPS on the octagon lattice (b). Then, we decompose octagon MPS from (b) to (c). The rank-3 tensor in (d) is the fixed-point tensor we will study here. (e) The geometry of the corresponding 3-point correlation functions.

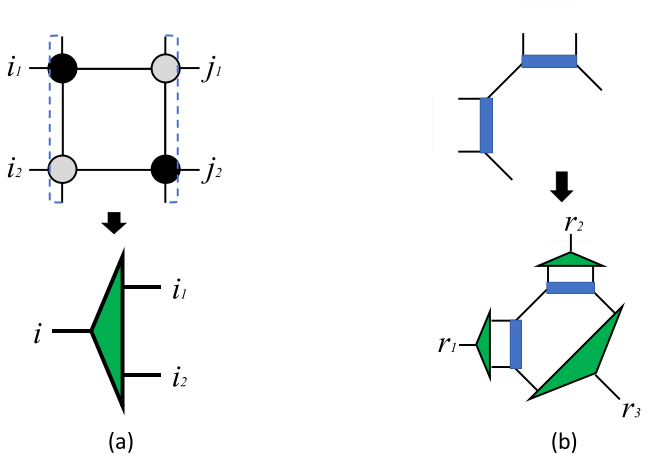

FIG. 17. (a) We choose the eigenstates of the transfer matrix in as our basis. (b) We then project the rank-3 fixed-point tensors on to these basis.

2×2 transfer matrix as shown in Fig. 17(a), and apply the eigenvalue decomposition:

$$M_{(i_1 i_2)(j_1 j_2)} = \sum_k U_{(i_1 i_2)k} \lambda_k [U^{-1}]_{k(i_1 i_2)}. \tag{15}$$

We use eigenvectors $U_{(i_1 i_2)i}$ as the basis for the fixed-point tensor, as shown in Fig. 17(b). As a result, the fixed-point tensor is projected onto the basis representing primary fields and their descendants.

2. *Operator product expansion (OPE) coefficient from the fixed-point tensor*

In Table V, we list the leading nonzero components of the fixed-point tensors of different q-state clock models at

TABLE V. A comparison of nonzero leading components of the fixed-point tensor of q-state clock models with $q = 7, 8, 9, 10$ at BKT critical point.

$T^{q=7}_{r_1 r_2 r_3}$	$T^{q=8}_{r_1 r_2 r_3}$	$T^{q=9}_{r_1 r_2 r_3}$	$T^{q=10}_{r_1 r_2 r_3}$	r_1	r_2	r_3
1.00000	1.00000	1.00000	1.00000	I	I	I
0.81215	0.81594	0.81555	0.81725	I	α	β
0.81215	0.81594	0.81555	0.81725	I	β	α
0.44178	0.44747	0.45242	0.45253	I	γ	δ
0.44178	0.44747	0.45242	0.45253	I	δ	γ
0.81215	0.81594	0.81555	0.81725	α	I	β
0.59058	0.59609	0.59756	0.59821	α	α	δ
0.74242	0.74698	0.74671	0.74901	α	β	I
0.45419	0.46021	0.49495	0.46479	α	δ	α
0.81215	0.81594	0.81555	0.81725	β	I	α
0.74242	0.74698	0.74671	0.74901	β	α	I
0.59058	0.59609	0.59756	0.59821	β	β	γ
0.45419	0.46021	0.46369	0.46479	β	γ	β
0.44178	0.44747	0.45242	0.45253	γ	I	δ
0.45419	0.46021	0.46369	0.46479	γ	β	β
0.30919	0.31491	0.32114	0.32120	γ	δ	I
0.44178	0.44747	0.45242	0.45253	δ	I	γ
0.45419	0.46021	0.46369	0.46479	δ	α	α
0.30919	0.31491	0.32114	0.32120	δ	γ	I

BKT critical point. Here we normalize the largest component $T_{III} = 1$. We use $I, \alpha, \beta, \gamma, \delta, \lambda$, and η to represent the leading primary fields (0,0), (1,0), $(-1, 0)$, (2,0), $(-2, 0)$, (3,0), and $(-3, 0)$.

It is well known that the fusion rule of the primary fields in compactified boson theory satisfies:

$$[\phi_{e_1,m_1}] \times [\phi_{e_2,m_2}] = [\phi_{e_1+e_2,m_1+m_2}], \tag{16}$$

where $[\phi_{e,m}]$ is a conformal family generated by primary field $\phi_{e,m}$ with conformal dimension $((e/R + mR/2)^2/2, (e/R - mR/2)^2/2)$. In particular, the primary field with $m = 0$ $\phi_{e,0}$ is just the vertex operator and it can be written as

$$\phi_{e,0}(z, \bar{z}) = e^{ie\varphi(z,\bar{z})/R}, \tag{17}$$

with $\varphi(z, \bar{z})$ is just the free boson field. The 3-point function has a pretty simple form:

$$\begin{aligned}&\langle \phi_{e_1,0}(z_1, \bar{z}_1)\phi_{e_2,0}(z_2, \bar{z}_2)\phi_{e_3,0}(z_3, \bar{z}_3)\rangle \\ &= \frac{C_{123}}{|z_{12}|^{\Delta_1+\Delta_2-\Delta_3}|z_{23}|^{\Delta_2+\Delta_3-\Delta_1}|z_{31}|^{\Delta_3+\Delta_1-\Delta_2}},\end{aligned} \tag{18}$$

where C_{123} is the OPE coefficients, which equals 1 for $e_1 + e_2 + e_3 \neq 0$ and vanishes for $e_1 + e_2 + e_3 = 0$. $|z_{12}| \equiv |z_1 - z_2|$, and the scaling dimension $\Delta_i = \frac{e_i^2}{R^2}$. We note that in general only leading primary fields in our numerical fixed-point tensor can satisfy the fusion rule since we use the Z_q symmetry to approximate the U(1) symmetry in the gauge fixing procedure, and with increasing q, more and more primary fields with correct fusion rules can be resolved numerically. Although we believe that the emergent U(1) must be present for all finite q with $q > 4$, it is in general very hard to find the proper gauge choice for small q, especially for $q = 5$ and $q = 6$.

Next, we can try to fit our numerical fixed-point tensor by using the 3-point correlation function Eq. (18). Let $z_{13} = \lambda_1 x$, $z_{23} = \lambda_2 x$, $z_{12} = \lambda_3 x$. We can rewrite the right-hand side of Eq. (18) as

$$\begin{aligned}&\frac{C_{123}}{(\lambda_1 x)^{\Delta_1+\Delta_3-\Delta_2}(\lambda_2 x)^{\Delta_2+\Delta_3-\Delta_1}(\lambda_3 x)^{\Delta_1+\Delta_2-\Delta_3}} \\ &= C_{123}\left(\frac{\lambda_2}{\lambda_1\lambda_3 x}\right)^{\Delta_1}\left(\frac{\lambda_1}{\lambda_2\lambda_3 x}\right)^{\Delta_2}\left(\frac{\lambda_3}{\lambda_1\lambda_2 x}\right)^{\Delta_3} \\ &\equiv C_{123} l_1^{\Delta_1} l_2^{\Delta_2} l_3^{\Delta_3},\end{aligned} \tag{19}$$

with $l_1 = \frac{\lambda_2}{\lambda_1\lambda_3 x}$, $l_2 = \frac{\lambda_1}{\lambda_2\lambda_3 x}$, and $l_3 = \frac{\lambda_3}{\lambda_1\lambda_2 x}$, respectively. From the geometry of the square lattice, we conjecture that our rank-3 fixed-point tensor can be regarded as 3-point correlation (at least for primary fields) function on the vertex of an isosceles right triangle on the complex plane, as seen in Fig. 16(e). Thus we can choose $\lambda_1 = \lambda_2 = \lambda_3/\sqrt{2} = 1$ and Eq. (19) can be simplified as

$$C_{123} l_1^{\Delta_1} l_2^{\Delta_2} l_3^{\Delta_3} \equiv C_{123} l^{\Delta_1} l^{\Delta_2} (2l)^{\Delta_3}, \tag{20}$$

where $l = \frac{1}{\sqrt{2}x}$ is a fundamental inverse length scale. For $q = 10$ model at the temperature T_{c2}, the nonzero leading components of fixed-point tensor are given by Table VI. If we fit our data with Eq. (20), we find

$$\begin{aligned}\Delta_{(\pm1,0)} &= 0.12684, \\ \Delta_{(\pm2,0)} &= 0.50869, \\ \Delta_{(\pm3,0)} &= 1.17789,\end{aligned} \tag{21}$$

which match well with the results from our previous transfer matrix calculation, with $\Delta_{(\pm1,0)} = 0.12539$, $\Delta_{(\pm2,0)} = 0.50158$, and $\Delta_{(\pm3,0)} = 1.12851$ (the corresponding compactification radius $R = 2.82402$). The fundamental length scale can also be fitted as $x = 2.23035$, and the corresponding OPE coefficients are listed in Table VII. The relative error of our fitting is estimated as

$$\sqrt{\frac{\sum_N \left[\left||T_{r_1r_2r_3}| - C_{123} l^{\Delta_1} l^{\Delta_2} (2l)^{\Delta_3}\right|/|T_{r_1r_2r_3}|\right]^2}{N}}, \tag{22}$$

where N is the total number of components in our consideration. We find the fitting error is around 4.0×10^{-3}. Thus, we conclude that the fixed-point tensor can be well described by the 3-point function (at least for primary fields) and the OPE coefficients can be read out directly.

TABLE VI. Leading nonzero components of the fixed-point tensor of $q = 10$ model at BKT critical point T_{c2}.

$T_{r_1r_2r_3}$	r_1	r_2	r_3	$T_{r_1r_2r_3}$	r_1	r_2	r_3
1.00000	I	I	I	0.45253	γ	I	δ
0.81725	I	α	β	0.30155	γ	α	η
0.81725	I	β	α	0.46479	γ	β	β
0.45253	I	γ	δ	0.32120	γ	δ	I
0.45253	I	δ	γ	0.15522	γ	η	α
0.17675	I	λ	η	0.45253	δ	I	γ
0.17675	I	η	λ	0.46479	δ	α	α
0.81725	α	I	β	0.30155	δ	β	λ
0.59820	α	α	δ	0.32120	δ	γ	I
0.74901	α	β	I	0.15522	δ	λ	β
0.30155	α	γ	η	0.17675	λ	I	η
0.46479	α	δ	α	0.20004	λ	β	δ
0.20004	α	η	γ	0.15522	λ	δ	β
0.81725	β	I	α	0.08449	λ	η	I
0.74901	β	α	I	0.17675	η	I	λ
0.59820	β	β	γ	0.20004	η	α	γ
0.46479	β	γ	β	0.15522	η	γ	α
0.30155	β	δ	λ	0.08449	η	λ	I
0.20004	β	λ	δ				

C. Fixed-point tensor for general cases

In fact, the above structure of fixed-point tensor holds for the whole critical phase between T_{c1} and T_{c2}. In the following, we further study the fixed-point tensor for the $q = 10$ case at different temperatures. Table VIII shows that all the OPE coefficients are very close to 1, as expected from the compactified boson theory. Table IX shows the comparison between the scaling dimensions read from the fixed-point tensor and from the direct calculation of transfer matrix. We see that they also match very well.

Therefore, we find very strong evidence that the fixed-point tensor can be described by three-point correlation function for

TABLE VII. Fitting OPE coefficients in Eq. (18) of $q = 10$ model at temperature $T = T_{c2}$, we see that they approach the expected value 1.

$C_{r_1r_2r_3}$	r_1	r_2	r_3	$C_{r_1r_2r_3}$	r_1	r_2	r_3
1.00000	I	I	I	1.00000	γ	I	δ
1.00000	I	α	β	1.01105	γ	α	η
1.00000	I	β	α	1.00350	γ	β	β
1.00000	I	γ	δ	1.00000	γ	δ	I
1.00000	I	δ	γ	0.99779	γ	η	α
1.00000	I	λ	η	1.00000	δ	I	γ
1.00000	I	η	λ	1.00350	δ	α	α
1.00000	α	I	β	1.01105	δ	β	λ
1.00023	α	α	δ	1.00000	δ	γ	I
1.00000	α	β	I	0.99779	δ	λ	β
1.01105	α	γ	η	1.00000	λ	I	η
1.00350	α	δ	α	0.99590	λ	β	δ
1.01105	α	η	γ	0.99779	λ	δ	β
1.00000	β	I	α	1.00000	λ	η	I
1.00000	β	α	I	1.00000	η	I	λ
1.00023	β	β	γ	0.99590	η	α	γ
1.00350	β	γ	β	0.99779	η	γ	α
1.01105	β	δ	λ	1.00000	η	λ	I
0.99590	β	λ	δ				

primary fields. Such a structure also explains why loop-TNR is a very accurate algorithm for critical systems since primary fields with higher scaling dimensions will lead to a rapid decay for the corresponding tensor components. We also find that the components for descendant fields are always smaller than the corresponding primary field in the fixed-point tensor. We believe this is also because descendant fields will have bigger scaling dimensions. However, the explicit fixed-point tensor structure for descendant fields is rather complicated and we will leave this problem in our future study.

TABLE VIII. OPE coefficients in Eq. (18) fitting from the data of model $q = 10$ on different temperature.

$C^{t=0.70}_{r_1r_2r_3}$	$C^{t=0.76}_{r_1r_2r_3}$	$C^{t=0.80}_{r_1r_2r_3}$	r_1	r_2	r_3
1.00000	1.00000	1.00000	I	I	I
1.00000	1.00000	1.00000	I	α	β
1.00000	1.00000	1.00000	I	β	α
1.00000	1.00000	1.00000	I	γ	δ
1.00000	1.00000	1.00000	I	δ	γ
1.00000	1.00000	1.00000	α	I	β
0.99967	0.99961	0.99955	α	α	δ
1.00000	1.00000	1.00000	α	β	I
1.00016	1.00015	1.00010	α	δ	α
1.00000	1.00000	1.00000	β	I	α
1.00000	1.00000	1.00000	β	α	I
0.99967	0.99961	0.99955	β	β	γ
1.00016	1.00015	1.00010	β	γ	β
1.00000	1.00000	1.00000	γ	I	δ
1.00016	1.00015	1.00010	γ	β	β
1.00000	1.00000	1.00000	γ	δ	I
1.00000	1.00000	1.00000	δ	I	γ
1.00016	1.00015	1.00010	δ	α	α
1.00000	1.00000	1.00000	δ	γ	I

TABLE IX. Scaling dimension of the first 3 levels reads by fitting fixed-point tensor with 3-point function of CFT and from the calculation of transfer matrix.

Temperature	Δ_1	Δ_2	Δ_3	Fitting radius R
From fixed-point tensor				
0.70	0.06941	0.27824	0.62659	3.79267
0.72	0.07228	0.28971	0.65169	3.72312
0.74	0.07532	0.30182	0.67813	3.64573
0.76	0.07851	0.31456	0.70589	3.57106
0.78	0.08191	0.32813	0.73536	3.49684
0.80	0.08566	0.34298	0.76683	3.41513
From transfer matrix				
0.70	0.06940	0.27795	0.62510	3.79498
0.72	0.07217	0.28845	0.65024	3.72290
0.74	0.07508	0.30057	0.67854	3.64905
0.76	0.07830	0.31386	0.70314	3.57325
0.78	0.08178	0.32827	0.73366	3.49727
0.80	0.08571	0.34675	0.76734	3.41494

V. CONCLUSIONS AND DISCUSSIONS

In summary, we use loop-TNR algorithm to study the phase transition properties of the q-state clock model. For $q < 5$ models, we compute the central charge and scaling dimensions at the self-dual critical points and find perfect agreement with previous CFT predictions. For $q > 5$ models, we determine the critical temperatures T_{c1} and T_{c2} for both phase transitions with very high precision. By further computing the central charge and scaling dimensions at T_{c1} and T_{c2}, we can further obtain the compactification radius R, which also perfectly agrees with the Z_q deformed sine-Gordon theory predictions. Interestingly, for big enough q, we find that the fixed-point tensor at T_{c2} converges to the same one (up to numerical errors) that describes the well known BKT transitions, and the corresponding OPE coefficients can also be read out directly.

For our future work, it will be of great interest to investigate the explicit expression of the infinite dimensional fixed-point tensor description for the compactified boson theory as well as general CFT. In fact, the fixed-point tensor provides us a purely algebraic way to describe CFT, which origins from a geometric perspective. Very recently, it has been shown that the p-adic CFT [42] admits an explicit finite dimensional tensor-network representation. It is somewhat not quite surprising since p-adic CFT has no descendant fields. The fixed-point tensor form for the descendant fields might tell us how geometry emerges from basic algebraic data.

ACKNOWLEDGMENTS

We are grateful to Ling-Yan Hung and Gong Cheng for very enlightening discussions for the structure of fixed-point tensors at critical points. This work is supported by funding from Hong Kong's Research Grants Council (GRF No. 14301219) and Direct Grant No. 4053409 from The Chinese University of Hong Kong.

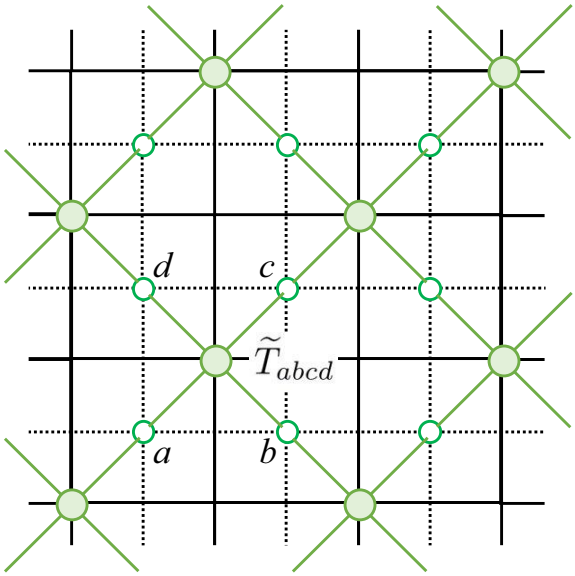

FIG. 18. Tensor-network representation of dual model, where the original lattice is shown by solid line and the dual lattice is shown by dash line.

APPENDIX A: FITTING CONFORMAL DATA FROM LOOP-TRG ALGORITHM

We read off conformal data from fixed-point tensor such as compactification radius R as follows:

We first choose the scaling dimensions of RG steps from 15–20. We note that for very small system size, the conformal data is not converged into the thermal dynamical limit, while for very big size, the truncation error will accumulate and eventually destroy the RG fixed-point tensor.

Then we use the first two lowest levels of scaling dimension for data fitting, since the accuracy of higher level scaling is not good enough as lower ones. We fit the compactification radius by minimizing the following cost function:

$$f(R) = \sum_{j=15}^{20}\left(\frac{1}{R^2} - l^1_{RGj}\right) + \sum_{j=15}^{20}\left(\frac{4}{R^2} - l^2_{RGj}\right),$$

where l^k_{RGj} is the data of kth level of scaling dimension in jth RG step.

APPENDIX B: COMPACTIFICATION RADIUS FOR $q = 5$ AND $q = 6$ MODELS AT SELF-DUAL POINT

In this section, we investigate the scaling dimensions and compactification radius R for the so-called self-dual point. The element tensor for dual model in Fig. 18, which is obtained by Kramers-Wannier transformation [37,43,44], could be expressed as

$$\widetilde{T}_{abcd} = \exp\frac{\beta}{2}(\cos\theta_a + \cos\theta_b + \cos\theta_c + \cos\theta_d) \times \delta_{\mathrm{mod(a+b+c+d,q)},0}. \tag{B1}$$

To determine the self-dual temperature, we compute the magnetization at different temperatures for both q-state model and its dual model. As seen in Fig. 19, the crossing point

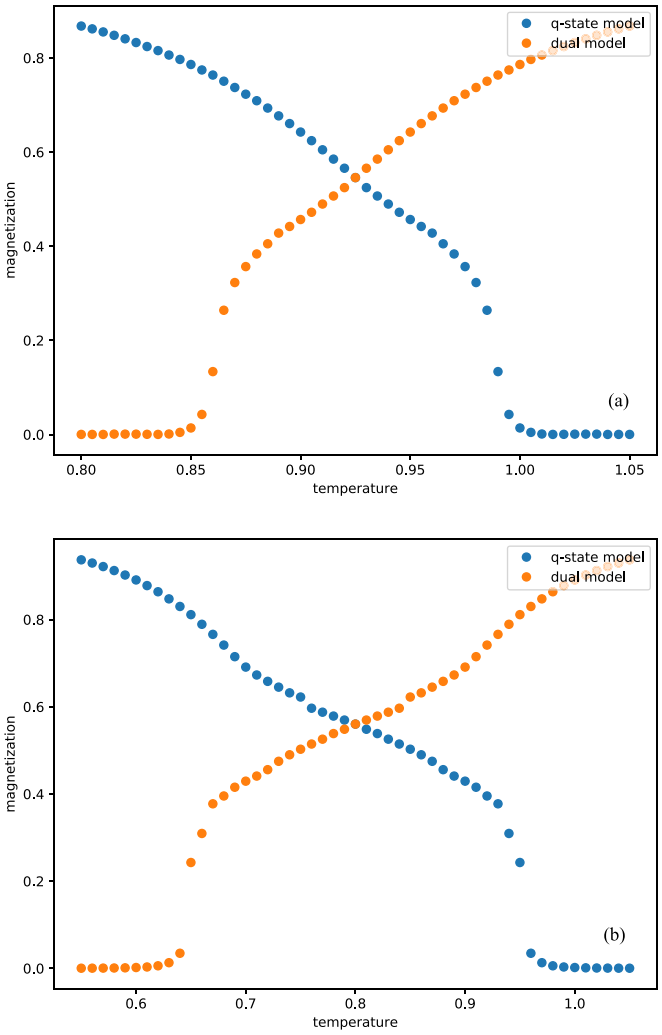

FIG. 19. Magnetization of q-state clock model with (a) $q = 5$, (b) $q = 6$, and their corresponding dual model.

corresponds to the dual temperature with $g_1 = g_2$. G. Ortiz *et al.* [45] demonstrated the existence of two critical points of q-state clock model in $q > 4$ cases in "bond-algebraic" approach, and investigated the self-dual points of different q model, which are comparable with our numerical results. Again, we can use the loop-TNR algorithm to compute the scaling dimensions (see in Fig. 20) and from the scaling dimension data, we can further fit the compactification R. In Table II, we compare our results with the theoretical predictions. Again, we find a perfect agreement for both $q = 5$ and $q = 6$ models.

APPENDIX C: TRANSITION TEMPERATURES AND COMPACTIFICATION RADIUS R FOR $q > 6$ MODELS

For models with $q > 6$, e.g., $q = 7, 8, 9$ we can also use the invariant quantity χ to determine the transition temperature for T_{c1} and T_{c2}, as seen in Figs. 21 and 22. In Figures 23–25, we also use the susceptibility peak method Eq. (12) to determine the BTK transition temperature T_{c2} with very high accuracy. Remarkably, we find that for $q > 6$, the fitting parameters a and b are already very close to those obtained

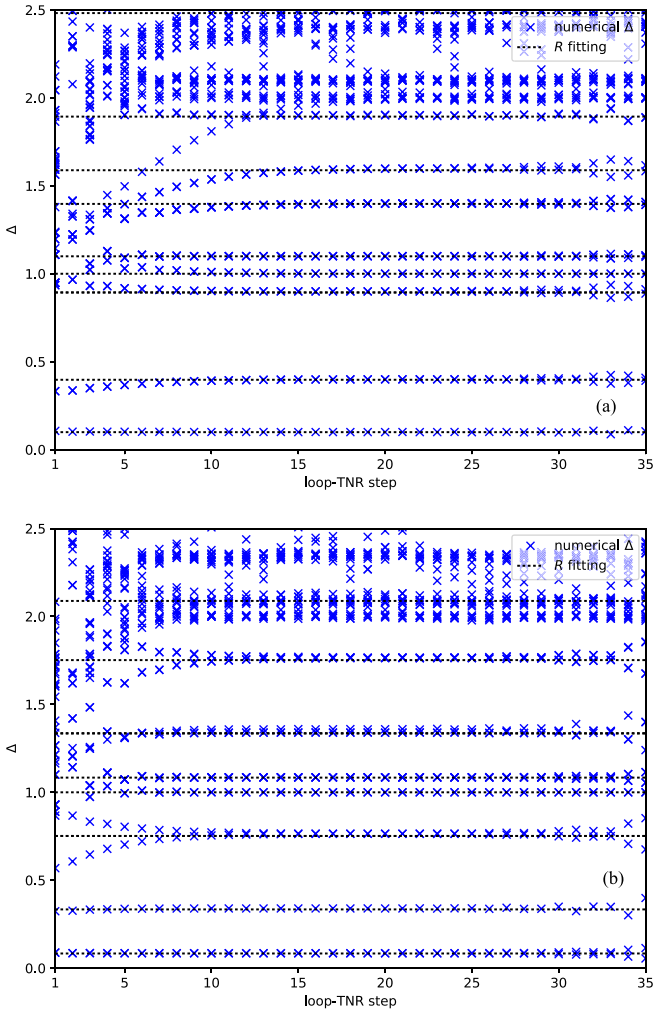

FIG. 20. Scaling dimension on self-dual point for (a) $q = 5$ and (b) $q = 6$ models, from which we can fit the compactification radius R of the compactified boson theory. We find that $R = 3.17354$ for $q = 5$ and $R = 3.46002$ for $q = 6$ model.

from classical XY model [38]. Finally, we use the loop-TNR algorithm to compute the scaling dimensions at both high- and low-temperature critical points as well as the self-dual point, as seen in Figs. 26–28. The corresponding compactification radius R can also be fitted by using Eq. (10).

APPENDIX D: IMPOSING C_4 ROTATIONAL SYMMETRY AND Z_q INTERNAL SYMMETRY IN LOOP-TNR ALGORITHM

In this Appendix we first give a short review for the loop-TNR algorithm [33]. Then we will discuss how to implement the C_4 lattice symmetry and the internal Z_q symmetry. Loop-TNR method mainly contains the following steps, as shown in Fig. 29. In general, there will be two types of tensors T_A and T_B on sublattices A and B during the renormalization process.

(i) In step (a), we apply entanglement filtering to remove the short-range entanglement [32], e.g., eliminating the corner double line (CDL) tensor. The CDL tensor only contains local entanglement and cannot be the fixed-point tensor describing

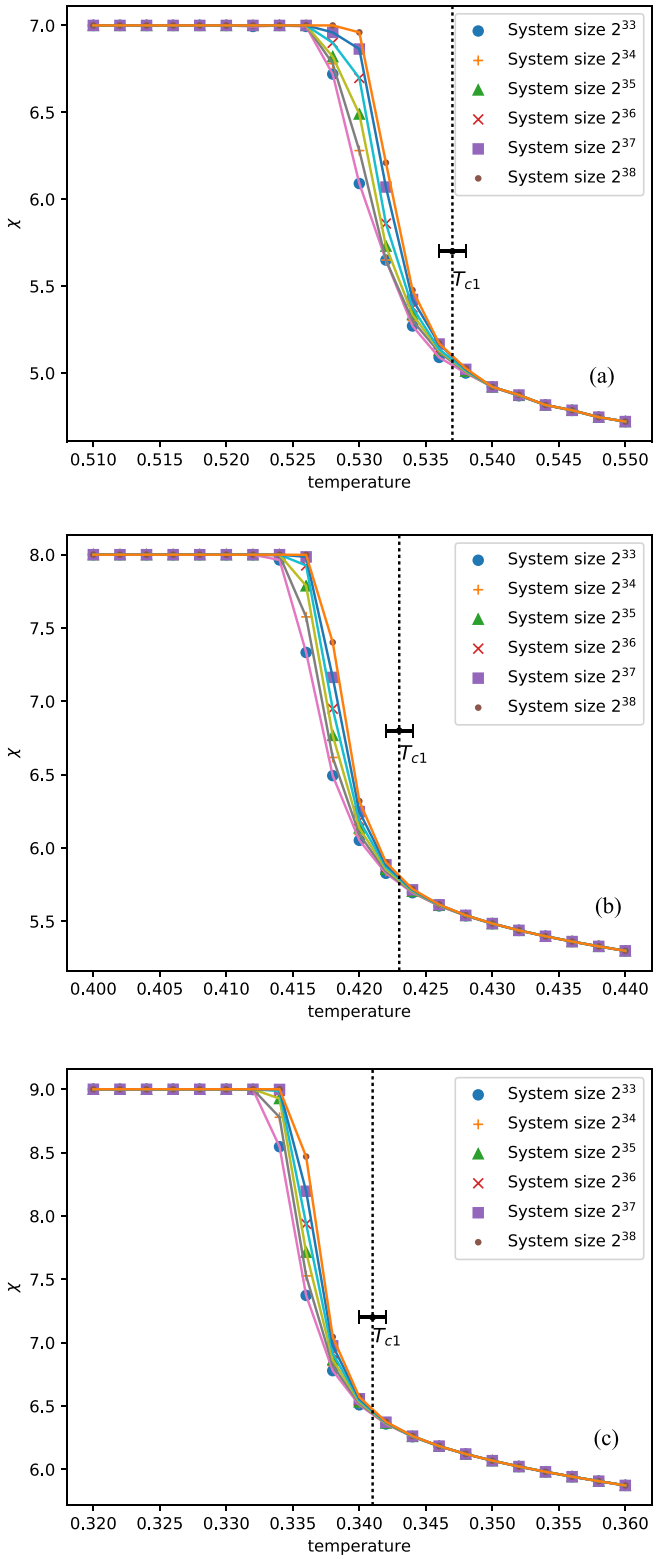

FIG. 21. Invariant quantity of for q-state clock model, (a), (b), and (c) for $q = 7, 8, 9$ respectively, around T_{c1}.

critical systems. References [31,33] give a detailed explanation on how to remove such short-range entanglement.

(ii) In step (b), we find 8 rank-3 tensor to form a octagon MPS to approximate the square MPS, as shown in Fig. 29(d). We are aiming to find the optimal choice of those 8 rank-3

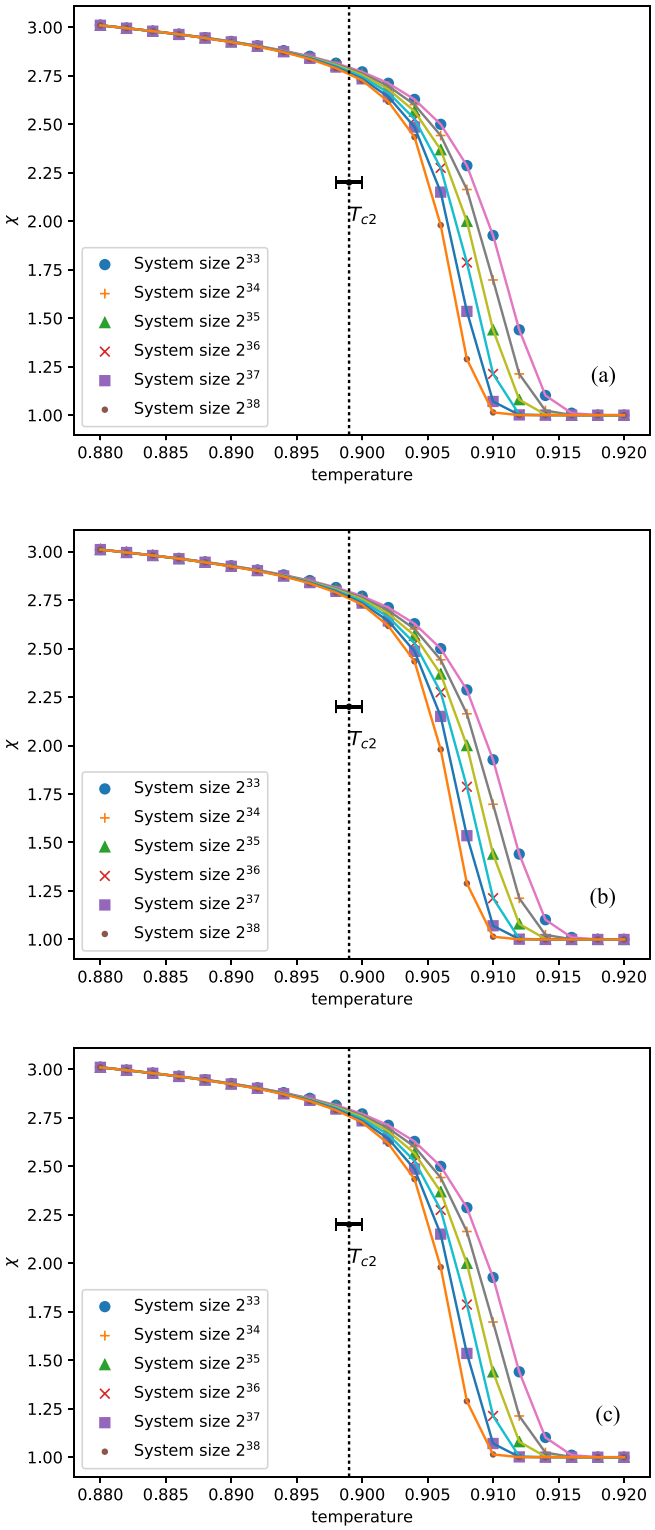

FIG. 22. Invariant quantity of for q-state clock model, (a), (b), and (c) for $q = 7, 8, 9$ respectively, around T_{c2}.

tensors $S_1, S_2, ...S_8$ to minimize the cost function in Fig. 29(d), which can be expressed as

$$C(S_1, S_2, \ldots, S_8) = \|T_A \cdot T_B \cdot T_A \cdot T_B - S_1 \cdot S_2 \cdot \cdots \cdot S_8\|^2. \tag{D1}$$

Since $S_1, S_2, ...S_8$ are independent variables, we can minimize this cost function with variational method. We denote the two

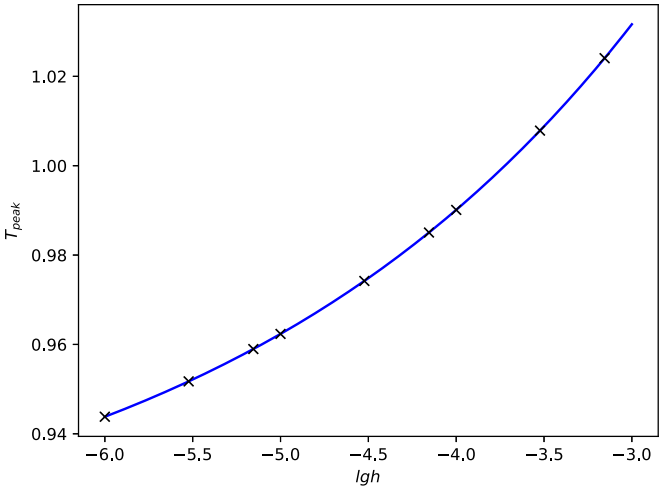

FIG. 23. Susceptibility peak temperature versus external field. For $q = 7$ model, we find that $T_c = 0.9065(5)$, $a = 0.4198$, $b = 0.1752$.

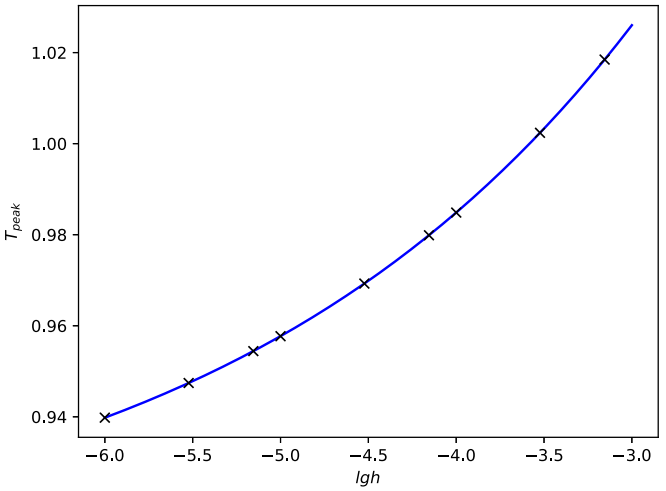

FIG. 24. Susceptibility peak temperature versus external field. For $q = 8$ model, we find that $T_c = 0.9051(5)$, $a = 0.4213$, $b = 0.1807$.

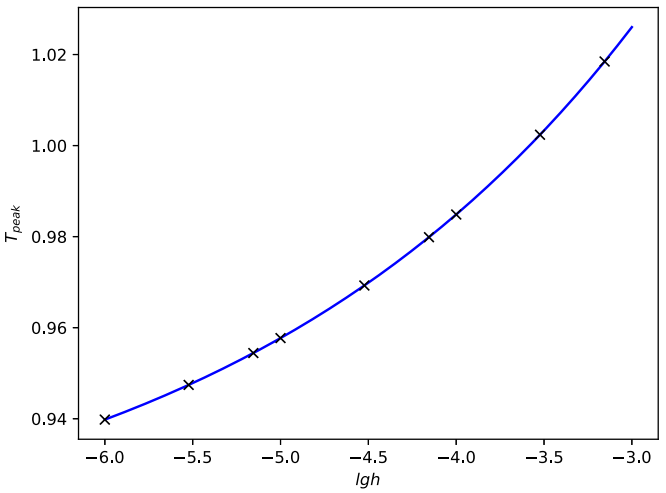

FIG. 25. Susceptibility peak temperature versus external field. For $q = 9$ model, we find that $T_c = 0.9051(5)$, $a = 0.4213$, $b = 0.1807$.

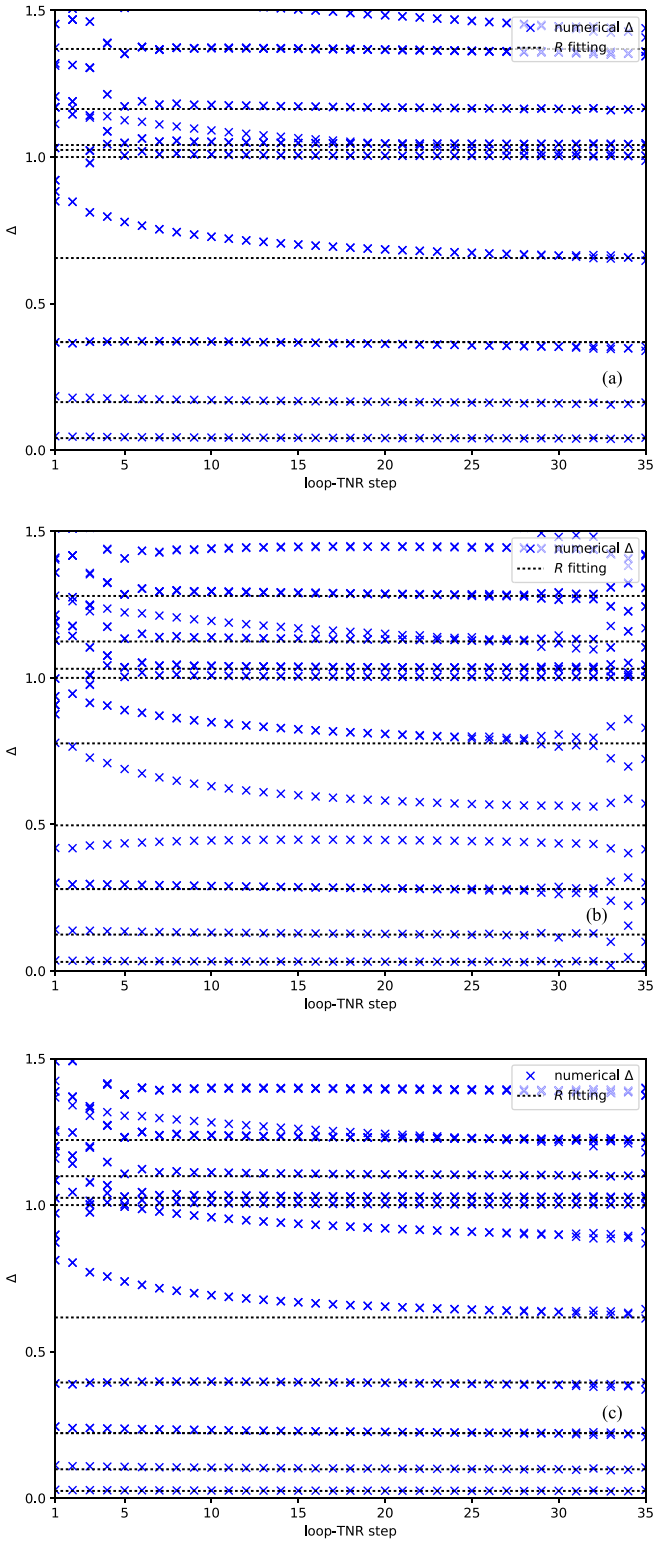

FIG. 26. Fitting of scaling dimensions at the critical point T_{c1}, (a), (b), and (c) for $q = 7, 8, 9$ model, from which we can read the character radius of the compactified boson theory.

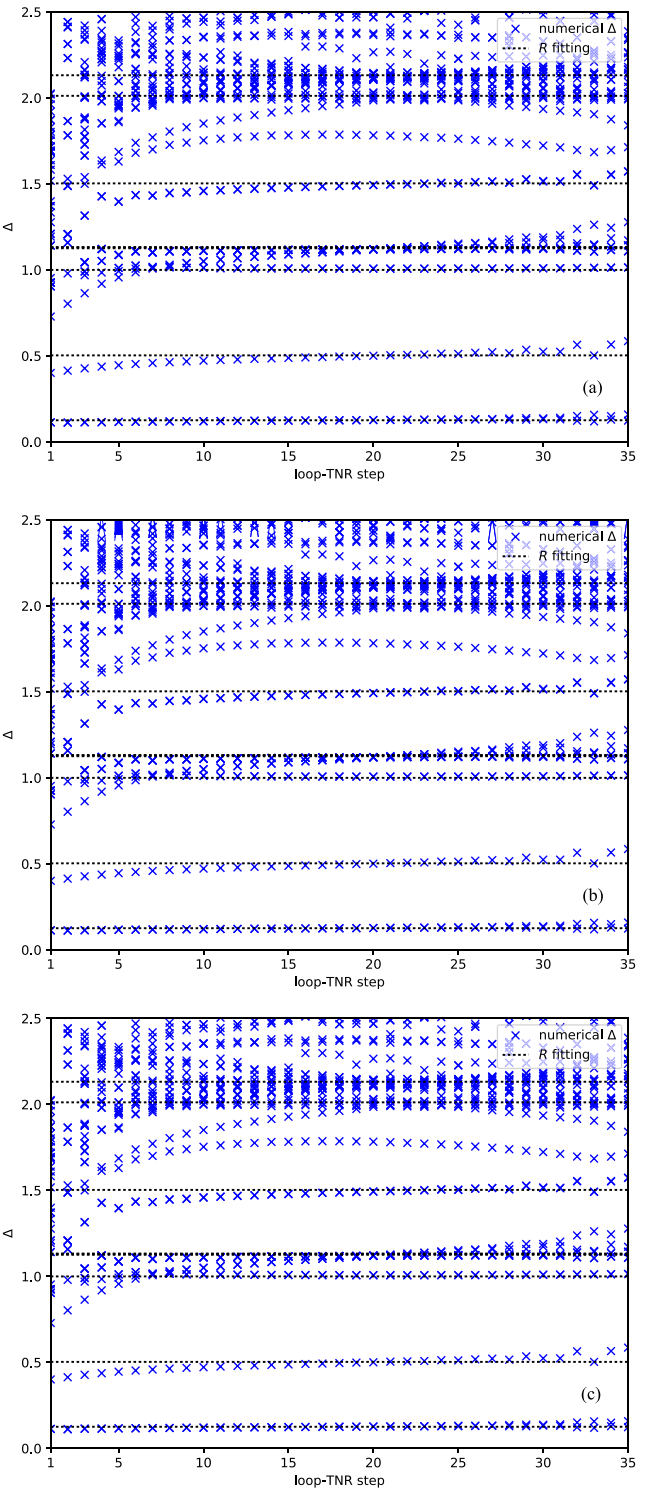

FIG. 27. Fitting of scaling dimensions at the critical point T_{c2}, (a), (b), and (c) for $q = 7, 8, 9$ model.

MPS's in above cost function as

$$|\Psi_A\rangle = T_A \cdot T_B \cdot T_A \cdot T_B,$$
$$|\Psi_B\rangle = S_1 \cdot S_2 \cdot \cdots \cdot S_8. \tag{D2}$$

Then, the cost function could be write down as

$$C(S_1, S_2, \ldots, S_8) = \langle\Psi_A|\Psi_A\rangle + \langle\Psi_B|\Psi_B\rangle - \langle\Psi_A|\Psi_B\rangle - \langle\Psi_B|\Psi_A\rangle. \tag{D3}$$

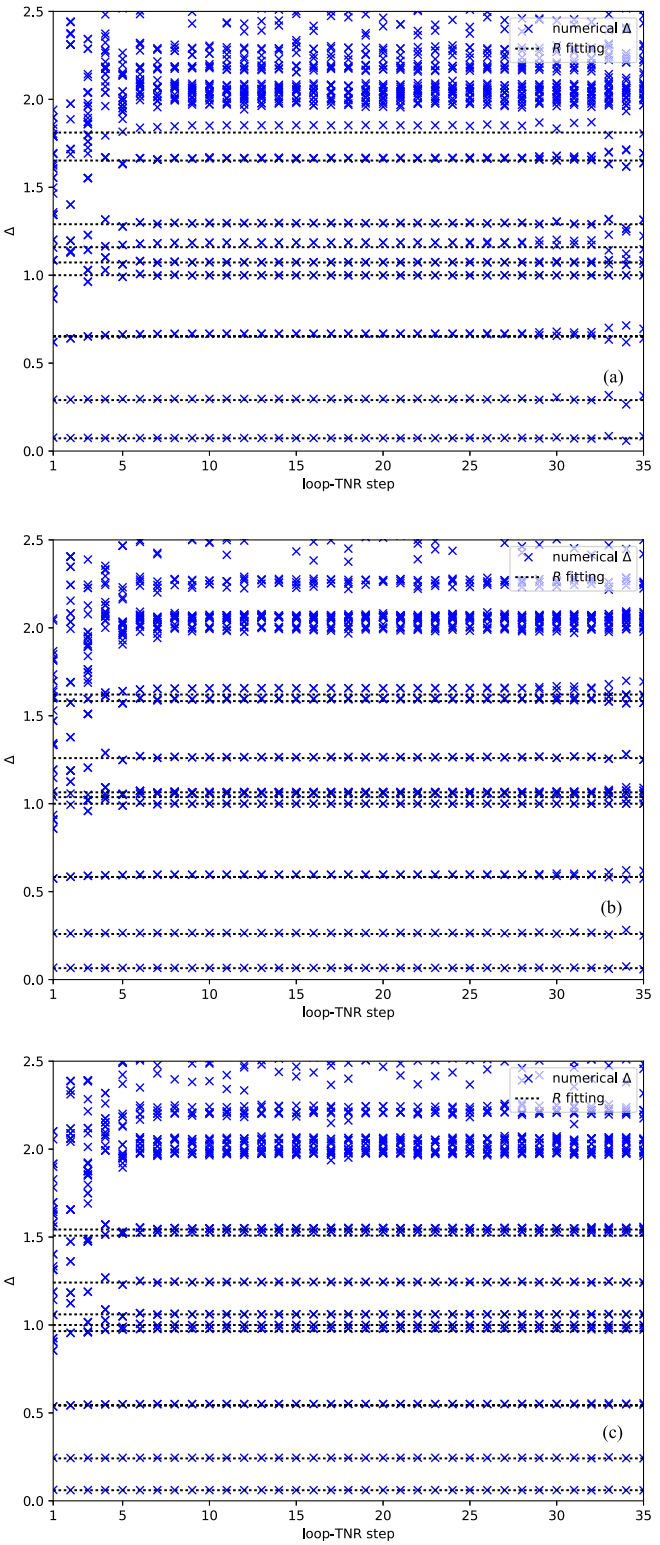

FIG. 28. Fitting of scaling dimensions at the self-dual point, (a), (b), and (c) for $q = 7, 8, 9$ model.

Taking variation on S_1, we get

$$\left.\frac{\delta C}{\delta S_1^\dagger}\right|_{S_2,S_3,..S_8} = \left\langle \frac{\delta \Psi_B}{\delta S_1^\dagger} \middle| \Psi_B \right\rangle - \left\langle \frac{\delta \Psi_B}{\delta S_1^\dagger} \middle| \Psi_A \right\rangle \equiv [N_1 \cdot S_1 - W_1]. \tag{D4}$$

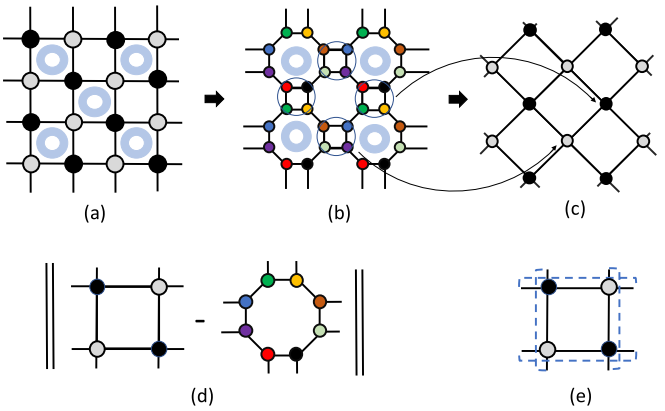

FIG. 29. Loop optimization procedure, in step (a), we apply entanglement filtering, and in step (b) we find the optimal S_i to minimize cost function as shown (d). (c) Then we trace the indices on the small square marked by the circle. (e) is gauge invariant quantity, which will be used as the overall normalization factor.

The minimum of $C(S_1)$ is given by the solution of the linear equation:

$$N_1 \cdot S_1 = W_1. \tag{D5}$$

The cost function (D5) and N_1, W_1 are illustrated in Fig. 30. After optimizing S_1, we can go on to the next site, and if we finish the optimization from S_1 to S_8, we finish one circle. By repeating this variational optimization, we can minimize the cost function.

(i) After minimizing the cost function, we trace the inner indices in the small circles, as shown in Fig. 29(b), and get the coarse-grained tensor T_A' and T_B', as in Fig. 29(c). Compared with the original tensor network, we find the tensor network composed of the renormalized tensor elements T_A' and T_B' (a) rotates an angle of $\pi/4$ and (b) the system size of the new network reduced to be half of the original. Then, we can start the new RG step from this tensor network.

(ii) We will normalize the tensor T_A and T_B in every RG step with the normalization factor as shown in Fig. 29(e).

1. Loop-TNR with C_4 lattice symmetry

To keep the lattice symmetry in the renormalization process, we need to find a octagon MPS with C_4 symmetry when minimizing the cost function in Fig. 31(d). We can construct this octagon MPS with the rank-4 block tensor M_{ijkl}, as shown

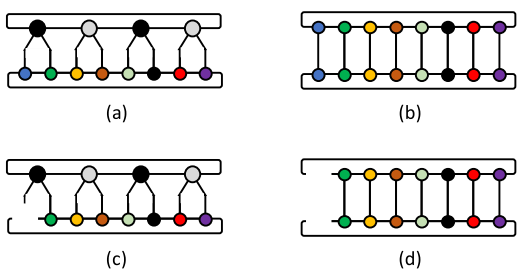

FIG. 30. Components of the cost function and its derivative. (a) is $\langle \Psi_A | \Psi_B \rangle$. (b) is $\langle \Psi_B | \Psi_B \rangle$. (c) and (d) are the quantity W_1 and N_1 in (D5), respectively.

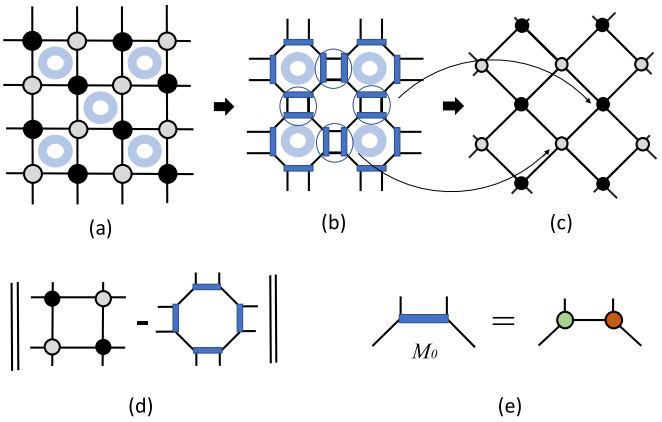

FIG. 31. Loop-TNR algorithm with C_4 lattice symmetry is similar with usual loop-TNR. Notice that the cost function in this case is nonlinear, so we need to use nonlinear optimization algorithm, such as conjugate gradient method.

in Fig. 31(b). Then we can use the conjugate gradient method to minimize the cost function:

$$C = \|T_A \cdot T_B \cdot T_A \cdot T_B - M \cdot M \cdot M \cdot M\|^2. \tag{D6}$$

After the optimization, we can use tensor M to build the renormalized tensor T'_A, T'_B, as shown in Fig. 31(c)

$$\begin{aligned} T^{A\prime}_{\text{ruld}} &= \sum_{ij} M_{ijrd} M_{jilu}, \\ T^{B\prime}_{\text{ruld}} &= \sum_{ij} M_{ijld} M_{jiru}. \end{aligned} \tag{D7}$$

Since the octagon network has C_4 symmetry, the coarse-grained tensor network on the square lattice marked by blue circle has the same C_4 symmetries.

The initial value of the tensor M is very important for the numerical accuracy. We can decompose tensor T_A and T_B by SVD method

$$\begin{aligned} T^A_{\text{ruld}} &\approx \sum_x S^1_{ldx} S^2_{rux} = \sum_x S^1_{rux} S^2_{ldx}, \\ T^B_{\text{ruld}} &\approx \sum_x S^1_{ulx} S^2_{drx} = \sum_x S^1_{drx} S^2_{ulx}. \end{aligned} \tag{D8}$$

Thus, the initial M is could be constructed as Fig. 31(e), with

$$M^0_{ijkl} = \sum_x S^1_{ixk} S^2_{xjl}. \tag{D9}$$

By keeping C_4 lattice symmetries in each iteration step, we have partially fixed the gauge of the building block M, which would be very important for studying the structure of the fixed-point tensor.

2. Loop-TNR with $Z(q)$ symmetry in Hamiltonian

As the original tensor element of q-state model T_{ijkl} contains $Z(q)$ symmetry, we can keep such a symmetry for every step in the loop-TNR algorithm [46]. As $Z(q)$ is a cyclic group, which contains group elements $\{I, g, g^2, ...g^{q-1}\}$, and the generator g has the q-dimension faithful representation

$$G_q = \begin{pmatrix} 0 & 0 & 0 & \dots & 0 & 1 \\ 1 & 0 & 0 & \dots & 0 & 0 \\ 0 & 1 & 0 & \dots & 0 & 0 \\ 0 & 0 & 1 & \dots & 0 & 0 \\ \dots & \dots & \dots & \dots & \dots & \dots \\ 0 & 0 & 0 & \dots & 1 & 0 \end{pmatrix}. \tag{D10}$$

It is easy to check that

$$\begin{aligned} T'_{\text{ruld}} &= \sum_{r'u'l'd'} [G_q]_{rr'} [G_q]_{uu'} [G_q]_{ll'} [G_q]_{dd'} T_{r'u'l'd'} \\ &= T_{\text{ruld}}. \end{aligned} \tag{D11}$$

In order to find out all the irreducible representation of the Z_q symmetry, we can just do eigenvalue decomposition for G_q,

$$G_q = V \Lambda V^{-1}, \tag{D12}$$

with eigenvalues $\Lambda_{nn} = \lambda_n = e^{2\pi i n/q}$, $n \in \{0, 1, 2, \dots, q-1\}$, and the components of the matrix V is given by

$$V_{mn} = \frac{e^{2\pi i m n/q}}{\sqrt{q}}, m, n \in \{0, 1, 2, \dots, q-1\}. \tag{D13}$$

Such that

$$G_q = V^{-1} \Lambda^{-1} V. \tag{D14}$$

Then, we define two tensors:

$$\begin{aligned} T^A_{\text{ruld}} &= \sum_{r'u'l'd'} [V^{-1}]_{rr'} [V^{-1}]_{uu'} [V^{-1}]_{ll'} [V^{-1}]_{dd'} T_{r'u'l'd'}, \\ T^B_{\text{ruld}} &= \sum_{r'u'l'd'} V_{rr'} V_{uu'} V_{ll'} V_{dd'} T_{r'u'l'd'}. \end{aligned} \tag{D15}$$

Obviously, tensor T^A and T^B form the same tensor network with T. In the new basis tensors T^A and T^B satisfy:

$$\begin{aligned} T^A_{\text{ruld}} &= \lambda_r \lambda_u \lambda_l \lambda_d T^A_{\text{ruld}}, \\ T^B_{\text{ruld}} &= \lambda_r^{-1} \lambda_u^{-1} \lambda_l^{-1} \lambda_d^{-1} T^B_{\text{ruld}}, \end{aligned} \tag{D16}$$

which implies that T^A_{ruld} and T^B_{ruld} only have nonzero components when $r + u + l + d \equiv 0 (\text{mod } q)$. Thus, tensors T^A and T^B are block diagonalized. It turns out that if we keep such block diagonalized property during RG process, i.e., in every RG step, we keep $r + u + l + d \equiv 0 (\text{mod } q)$, $Z(q)$ symmetry is preserved during loop-TNR process. In particular, we can keep $D_{\text{cut}} = nq$ (where n is an arbitrary integer), such that we can always construct a dimension nq by nq block diagonalized matrix Λ'

$$\Lambda' = \begin{pmatrix} \Lambda & \mathbf{0} & \dots & \mathbf{0} \\ \mathbf{0} & \Lambda & \dots & \mathbf{0} \\ \dots & \dots & \dots & \dots \\ \mathbf{0} & \mathbf{0} & \dots & \Lambda \end{pmatrix}. \tag{D17}$$

Obviously, Λ' is a representation of $Z(q)$ symmetry. So that $Z(q)$ symmetry is kept.

[1] V. L. Berezinskii, Destruction of long-range order in one-dimensional and two-dimensional systems having a continuous symmetry group. I. Classical systems, Zh. Eksp. Teor. Fiz. **59**, 907 (1970) [Sov. Phys. JETP **32**, 493 (1971)].

[2] J. M. Kosterlitz and D. J. Thouless, Long range order and metastability in two dimensional solids and superfluids. (Application of dislocation theory), J. Phys. C **5**, L124 (1972).

[3] J. M. Kosterlitz and D. J. Thouless, Ordering, metastability and phase transitions in two-dimensional systems, J. Phys. C **6**, 1181 (1973).

[4] H. Matsuo and K. Nomura, Berezinskii-Kosterlitz–Thouless transitions in the six-state clock model, J. Phys. A: Math. Gen. **39**, 2953 (2006).

[5] J. V. José, L. P. Kadanoff, S. Kirkpatrick, and D. R. Nelson, Renormalization, vortices, and symmetry-breaking perturbations in the two-dimensional planar model, Phys. Rev. B **16**, 1217 (1977).

[6] P. B. Wiegmann, One-dimensional fermi system and plane XY model, J. Phys. C **11**, 1583 (1978).

[7] J. Tobochnik, Properties of the q-state clock model for $q = 4$, 5, and 6, Phys. Rev. B **26**, 6201 (1982).

[8] S.-K Baek, P. Minnhagen, and B. J. Kim, True and quasi-long-range order in the generalized q-state clock model, Phys. Rev. E **80**, 060101(R) (2009).

[9] S. K. Baek and P. Minnhagen, Non-Kosterlitz-Thouless transitions for the q-state clock models, Phys. Rev. E **82**, 031102 (2010).

[10] Y. Kumano, K. Hukushima, Y. Tomita, and M. Oshikawa, Response to a twist in systems with Z_p symmetry: The two-dimensional p-state clock model, Phys. Rev. B **88**, 104427 (2013).

[11] C. Chatelain, DMRG study of the Berezinskii–Kosterlitz–Thouless transitions of the 2D five-state clock model, J. Stat. Mech. (2014) P11022.

[12] R. Krčmár, A. Gendiar, and T. Nishino, Phase transition of the six-state clock model observed from the entanglement entropy, arXiv:1612.07611.

[13] J. Chen, H.-J. Liao, H.-D. Xie, X.-J. Han, R.-Z. Huang, S. Cheng, Z.-C. Wei, Z.-Y. Xie, and T. Xiang, Phase transition of the q-state clock model: Duality and tensor renormalization, Chin. Phys. Lett. **34**, 050503 (2017).

[14] D.-H. Kim, Partition function zeros of the p-state clock model in the complex temperature plane, Phys. Rev. E **96**, 052130 (2017).

[15] Y. Chen, Z.-Y. Xie, and J.-F. Yu, Phase transitions of the five-state clock model on the square lattice, Chin. Phys. B **27**, 080503 (2018).

[16] S. Hong and D.-H. Kim, Logarithmic finite-size scaling correction to the leading fisher zeros in the p-state clock model: A higher-order tensor renormalization group study, Phys. Rev. E **101**, 012124 (2020).

[17] M. S. S. Challa and D. P. Landau, Critical behavior of the six-state clock model in two dimensions, Phys. Rev. B **33**, 437 (1986).

[18] J.-B. Zhang and D.-R. Ji, Monte Carlo simulation of the q-state clock model on a two-dimensional random lattice, Phys. Lett. A **151**, 469 (1990).

[19] A. Yamagata and I. Ono, Phase transitions of the 6-clock model in two dimensions, J. Phys. A: Math. Gen. **24**, 265 (1991).

[20] Y. Tomita and Y. Okabe, Probability-changing cluster algorithm for two-dimensional XY and clock models, Phys. Rev. B **65**, 184405 (2002).

[21] C.-O. Hwang, Six-state clock model on the square lattice: Fisher zero approach with Wang-Landau sampling, Phys. Rev. E **80**, 042103 (2009).

[22] A. F. Brito, J. A. Redinz, and J. A. Plascak, Two-dimensional XY and clock models studied via the dynamics generated by rough surfaces, Phys. Rev. E **81**, 031130 (2010).

[23] O. Borisenko, G. Cortese, R. Fiore, M. Gravina, and A. Papa, Numerical study of the phase transitions in the two-dimensional $Z(5)$ vector model, Phys. Rev. E **83**, 041120 (2011).

[24] O. Borisenko, V. Chelnokov, G. Cortese, R. Fiore, M. Gravina, and A. Papa, Phase transitions in two-dimensional $Z(N)$ vector models for $N > 4$, Phys. Rev. E **85**, 021114 (2012).

[25] R. P.-H. Wu, V.-C. Lo, and H.-T. Huang, Critical behavior of two-dimensional spin systems under the random-bond six-state clock model, J. Appl. Phys. **112**, 063924 (2012).

[26] S.-K. Baek, H. Mäkelä, P. Minnhagen, and B. J. Kim, Residual discrete symmetry of the five-state clock model, Phys. Rev. E **88**, 012125 (2013).

[27] S. Chatterjee, S. Puri, and R. Paul, Ordering kinetics in the q-state clock model: Scaling properties and growth laws, Phys. Rev. E **98**, 032109 (2018).

[28] T. Surungan, S. Masuda, Y. Komura, and Y. Okabe, Berezinskii–Kosterlitz–Thouless transition on regular and villain types of q-state clock models, J. Phys. A: Math. Theor. **52**, 275002 (2019).

[29] Z.-Q. Li, L.-P. Yang, Z.-Y. Xie, H.-H. Tu, H.-J. Liao, and T. Xiang, Critical properties of the two-dimensional q-state clock model, Phys. Rev. E **101**, 060105(R) (2020).

[30] M. Levin and C. P. Nave, Tensor Renormalization Group Approach to Two-Dimensional Classical Lattice Models, Phys. Rev. Lett. **99**, 120601 (2007).

[31] Z.-C. Gu and X.-G. Wen, Tensor-entanglement-filtering renormalization approach and symmetry-protected topological order, Phys. Rev. B **80**, 155131 (2009).

[32] G. Evenbly and G. Vidal, Tensor Network Renormalization, Phys. Rev. Lett. **115**, 180405 (2015).

[33] S. Yang, Z.-C. Gu, and X.-G. Wen, Loop Optimization for Tensor Network Renormalization, Phys. Rev. Lett. **118**, 110504 (2017).

[34] Z.-Y. Xie, H.-C. Jiang, Q.-J. N Chen, Z.-Y. Weng, and T. Xiang, Second Renormalization of Tensor-Network States, Phys. Rev. Lett. **103**, 160601 (2009).

[35] Z. Y. Xie, J. Chen, M. P. Qin, J. W. Zhu, L. P. Yang, and T. Xiang, Coarse-graining renormalization by higher-order singular value decomposition, Phys. Rev. B **86**, 045139 (2012).

[36] W. Janke, Logarithmic corrections in the two-dimensional XY model, Phys. Rev. B **55**, 3580 (1997).

[37] H. A. Kramers and G.H. Wannier, Statistics of the two-dimensional ferromagnet. Part I, Phys. Rev. **60**, 252 (1941).

[38] J.-F. Yu, Z.-Y. Xie, Y. Meurice, Y.-Z. Liu, A. Denbleyker, H.-Y. Zou, M.-P. Qin, J. Chen, and T. Xiang, Tensor renormalization group study of classical XY model on the square lattice, Phys. Rev. E **89**, 013308 (2014).

[39] H. Ueda, K. Okunishi, K. Harada, R. Krčmár, A. Gendiar, S. Yunoki, and T. Nishino, Finite-m scaling analysis of Berezinskii-Kosterlitz-Thouless phase transitions and entangle-

ment spectrum for the six-state clock model, Phys. Rev. E **101**, 062111 (2020).

[40] R. Krčmár, A. Gendiar, and T. Nishino, Entanglement-entropy study of phase transitions in six-state clock model, Acta Phys. Pol. A **137**, 598 (2020).

[41] G. Evenbly and G. Vidal, Local Scale Transformations on the Lattice with Tensor Network Renormalization, Phys. Rev. Lett. **116**, 040401 (2016).

[42] A. Bhattacharyya, L.-Y. Hung, Y. Lei, and W. Li, Tensor network and (p-adic) AdS/CFT, J. High Energy Phys. 01 (2018) 139.

[43] H. A. Kramers and G. H. Wannier, Statistics of the two-dimensional ferromagnet. Part II, Phys. Rev. **60**, 263 (1941).

[44] A. B. Zamolodchikov and M. I. Monastyrski, The Kramers-Wannier transformation for spin systems, JETP Lett. **2**, 196511 (1979) [Sov. Phys. JETP **50**, 167 (1979)].

[45] G. Ortiz, E. Cobanera, and Z. Nussinov, Dualities and the phase diagram of the p-clock model, Nucl. Phys. B **854**, 780 (2012).

[46] B. Bauer, P. Corboz, R. Orús, and M. Troyer, Implementing global Abelian symmetries in projected entangled-pair state algorithms, Phys. Rev. B **83**, 125106 (2011).